# LAYER-BY-LAYER ASSEMBLY OF CLAY-FILLED POLYMER

# NANOCOMPOSITE THIN FILMS

A Dissertation

by

WOO-SIK JANG

Submitted to the Office of Graduate Studies of
Texas A&M University
in partial fulfillment of the requirements for the degree of

DOCTOR OF PHILOSOPHY

December 2008

Major Subject: Mechanical Engineering

# LAYER-BY-LAYER ASSEMBLY OF CLAY-FILLED POLYMER

# NANOCOMPOSITE THIN FILMS

A Dissertation

by

WOO-SIK JANG

Submitted to the Office of Graduate Studies of
Texas A&M University
in partial fulfillment of the requirements for the degree of

DOCTOR OF PHILOSOPHY

Approved by:

| | |
|---|---|
| Chair of Committee, | Jaime C. Grunlan |
| Committee Members, | Richard B. Griffin |
| | Xinghang Zhang |
| | Michael J. McShane |
| Head of Department, | Dennis L. O'Neal |

December 2008

Major Subject: Mechanical Engineering

# ABSTRACT

Layer-by-Layer Assembly of Clay-filled Polymer Nanocomposite Thin Films.

(December 2008)

Woo-Sik Jang, B.S., Korea University; M.S., University of Colorado at Boulder

Chair of Advisory Committee: Dr. Jaime C. Grunlan

A variety of functional thin films can be produced using the layer-by-layer assembly technique. In this work, assemblies of anionic clay and cationic polymer were studied with regard to film growth and gas barrier properties. A simple, yet flexible robotic dipping system, for the preparation of these thin films, was built. The robot alternately dips a substrate into aqueous mixtures with rinsing and drying in between. Thin films of sodium montmorillonite clay and cationic polymer were grown and studied on poly(ethylene terephthalate) film or a silicon wafer. After 30 clay polymer bilayers were deposited, the resulting transparent film had an oxygen transmission rate (OTR) below 0.005 $cm^3/m^2/day/atm$. This low OTR, which is unprecedented for a clay-filled polymer composite, is believed to be due to a "brick wall" nanostructure comprised of completely exfoliated clay bricks in polymeric "mortar". The growth of polymer and clay assemblies is then shown to be controlled by altering the pH of polyethylenimine (PEI). Growth, oxygen permeability, and mechanical behavior of clay-PEI assemblies were studied as a function of pH in an effort to tailor the behavior of these thin films. Thicker deposition at high pH resulted in reduced oxygen permeability and lower modulus, which highlights the tailorability of this system.

# TABLE OF CONTENTS

# LIST OF FIGURES

# LIST OF TABLES

**CHAPTER I**

**INTRODUCTION**

**1.1 Background**

A variety of functional thin films can be produced using the layer-by-layer (LbL) assembly technique [1-2]. LbL-based thin films are currently being evaluated for a variety of applications that include drug delivery [3], molecular sensing [4], solid battery electrolytes [5], photovoltaics [6], and membranes [7]. Thin films, typically < 1μm thick, are created by alternately exposing a substrate to positively and negatively-charged molecules or particles, as shown in Figure 1. In this case, steps 1 − 4 are continuously repeated until the desired number of "bilayers" (or cationic-anionic pairs) is deposited. Each individual layer may be 1 − 100+ nm thick depending on chemistry [8], molecular weight [9], temperature [10], counter ion [11], ionic strength [12], and pH [13] of the species being deposited. This deposition technique has the ability to control the coating thickness down to the nm-level, easily insert variable thin layers without altering the process, economically use raw materials (due to their thin nature), self-heal, and be processed under ambient conditions. These films often have properties that are superior to comparable thick films (>>1μm). Furthermore, these films are often transparent, which opens up applications not available to comparable bulk films (e.g., food wrap). Altering the order and composition of layers provides limitless opportunity for new functionality.

---

Dissertation style and format follow those of Thin Solid Films.
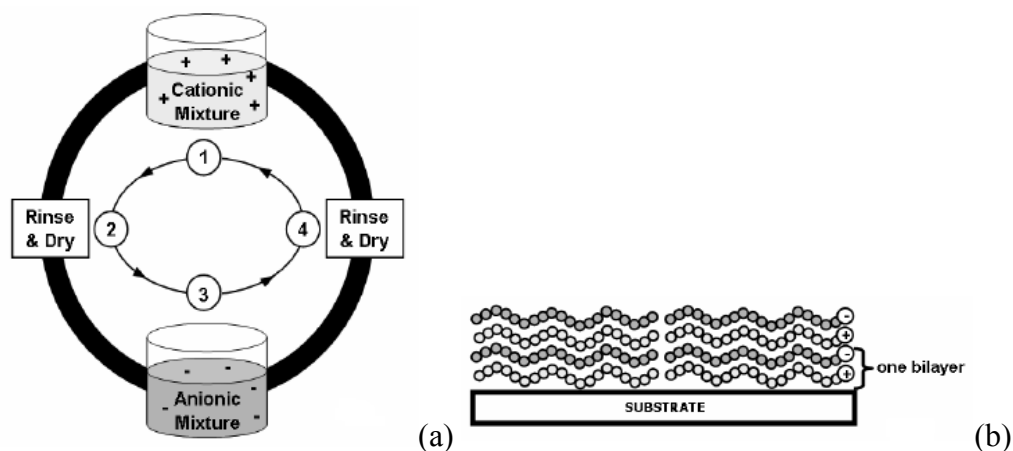
**Figure 1.** Schematic of layer-by-layer deposition process used to prepare functional thin films (a). Steps 1 – 4 are repeated until the desired number of bilayers are generated on a substrate (b).

## 1.2 Objectives and Dissertation Outline

The ultimate goal of the present work is to understand and improve the oxygen barrier of clay-based assemblies through the study of film growth and nanostructure. Byproducts of this research include building an automated dipping system, measuring mechanical properties, and characterizing the dielectric properties of clay-based assemblies. It is hoped that this work will result in a low cost, transparent and more flexible barrier film than is currently available for a variety of packaging applications (e.g., food and flexible electronics).

It is well established that impermeable clay platelets make the diffusion length longer through a polymer matrix by creating a tortuous path that reduces the oxygen transmission rate (OTR) [14-17]. The tortuous path concept was initially proposed by Nielsen [15] and further developed by Cussler [17] and others [18-21]. With regard to the study of LbL assemblies with clay, the key tasks include:

1. Measuring the OTR of clay-based LbL assemblies as a function of bilayers deposited and polymer charge density.

2. Characterizing film growth with ellipsometry and a quartz crystal microbalance (QCM).

3. Evaluating nanostructure with electron microscopy (SEM, TEM) and atomic force microscopy (AFM).

4. Correlating barrier behavior to established models that explain the observed behavior.

Chapter II is a literature review of LbL assembly and current oxygen barrier systems. An in depth review of the physical and chemical concepts of LbL assembly, and the types of functional films that can be produced, is provided. A review of current barrier technologies and several theories dealing with the tortuous pathway concept is also described in detail.

Chapter III describes the automated dipping system developed for this project. Many of these functional thin films require more than ten bilayers, or twenty total dipping cycles, to achieve a desired property. With many systems requiring dip times of five minutes or more, this process is too time consuming and prone to human error. The automated system is capable of producing tens of bilayers in a reproducible manner without constant supervision. This system is compared with other automated systems for layer-by-layer assembly. The control system and programming software are also described.

Chapter IV examines the barrier behavior of a model clay-based film. Layer-by-layer assemblies, built using a cationic polyacrylamide and natural montmorillonite clay, were studied as a means to produce a thin film with barrier properties that are unrivaled by conventional technologies. Oxygen transmission rate was measured along with film

thickness, microstructure, and surface morphology. This study lays the groundwork that is built upon in Chapter V, where OTR was tailored using pH.

Chapter V examines the influence of polymer charge density and clay type on oxygen barrier. Polyethylenimine (PEI), a weak polycation, has a pH adjustable charge density [22-24]. Low charge density makes the polymer highly coiled and this causes thicker deposition, while high charge density straightens the polymer chain due to strong self-repulsion, which leads to thinner deposition. Figure 2 highlights this pH-dependence for PEI, which has low charge density at high pH and high charge density at low pH [2].



(a)

(b)
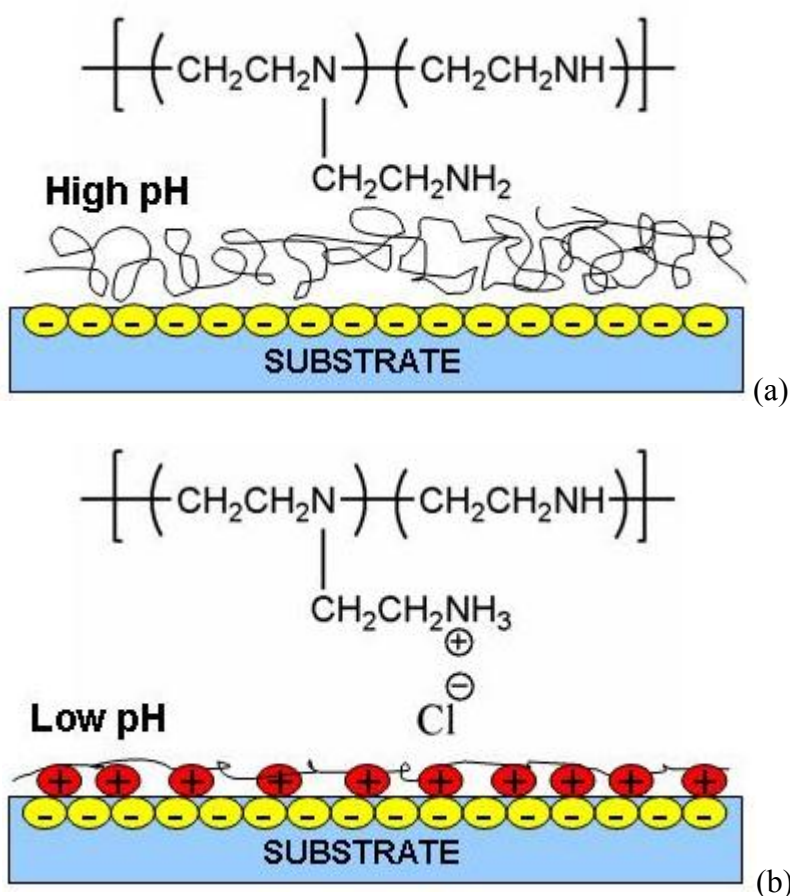
**Figure 2.** Weakly charged PEI at a high pH deposits thickly (a) and strongly charged PEI at a low pH deposits thinly (b).

 Chapter VI provides conclusions and future directions for clay-based assemblies, including their possible use as a flame retardant coating for foam and dielectric layer for thin film capacitors.

## CHAPTER II

## LITERATURE REVIEW

### 2.1 Layer-by-Layer Assembly

The Langmuir-Blodgett technique, which applies amphiphilic monolayers from a solution surface onto a substrate with simple dipping, was the precursor to layer-by-layer (LbL) assembly [25]. Iler was the first to perform true layer-by-layer assembly using charged particles [26]. Decher and coworkers later refined and further developed the LbL method [25, 27-29], which is more practical than Langmuir-Blodgett deposition. Ease of layer deposition and tailorability of film composition has led to numerous applications for LbL assemblies. For many practical applications, accurate thickness characterization and tailoring is necessary. In order for this to occur, the attraction between ingredients, the driving force for the LbL assembly, needs to be studied [28]. Film growth and functionalities of LbL-deposited thin films are reviewed here, followed by a discussion of barrier theories and current barrier technologies.

2.1.1 Film Growth

Layer-by-layer assemblies typically grow linearly [27, 29-31] or exponentially [12, 32-34]. Decher and his collaborators conducted thorough studies on linear growth [27, 29-31]. Strong cationic polyelectrolytes, such as poly(diallyldimethylammonium chloride) (PDDA) and poly(allylamine hydrochloride) (PAH), were combined with strongly anionic poly(styrene sulfonate) (PSS) for these studies. These polyelectrolytes are fully charged and this "strong" charge density results in relatively extended polymer

chains due to self-repulsion. Figure 3 shows how highly charged polymer chains will result in thinner laters that better cover the substrate surface relative to the more coiled, low charge density polymers.
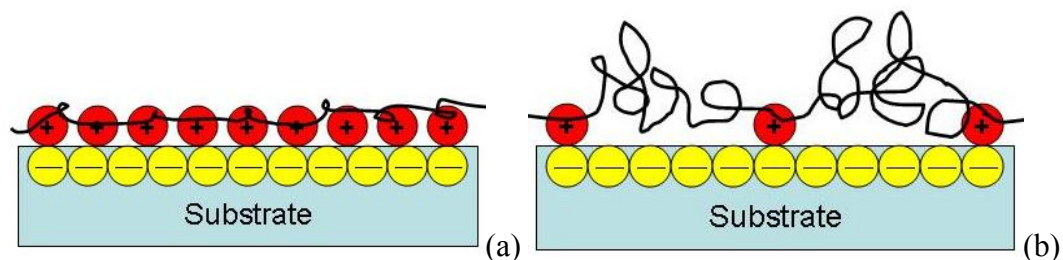


**Figure 3.** Fully charged polyelectrolytes result in a straightened polymer chain (a) while weakly charged polyelectrolytes results in a more coiled polymer chain (b).

In the case of the PAH/PSS system, small angle X-ray diffraction (SAXS) was used to accurately characterize the buildup of consecutive multilayers [27]. As seen in Figure 4, the thickness of individual layers was back-calculated by correlating the observed Kiessig fringes to the number of layers deposited. These early studies clearly demonstrated the linear growth of LbL assembly done with strong polyelectrolytes (Figure 4(b) was an early example).

(a)



(b)
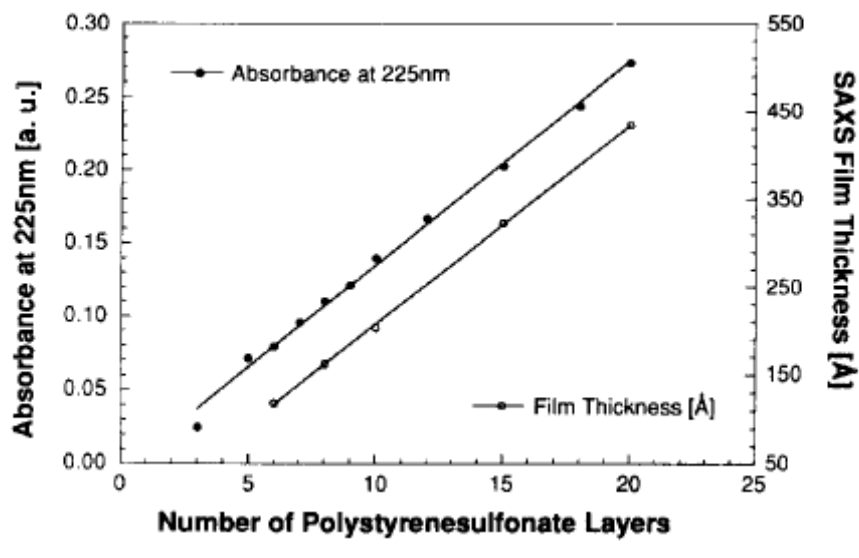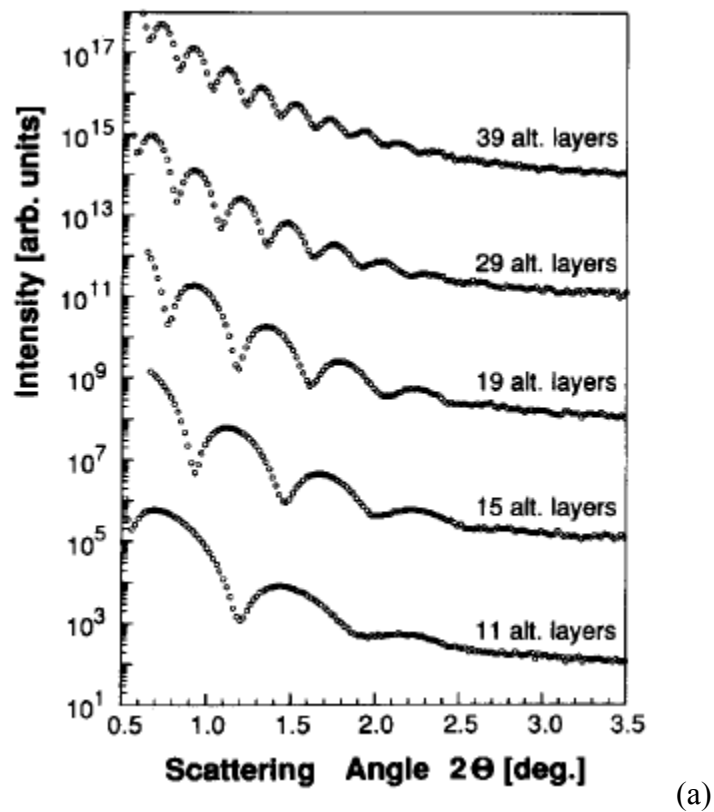
**Figure 4.** SAXS measurements of polystyrenesulfonate and polyallylamine (a) and the total film thickness back calculated from SAXS measurements (b) [27].

A variety of researchers later found that by altering the salt (e.g., NaCl) concentration in the polyelectrolyte deposition solutions, the thickness of each individual

layer could be tuned [12, 31, 35-43]. In the case of PAH/PSS, the addition of sodium chloride to the anionic PSS solution increases the thickness of PSS layers due to charge screening that makes the polymer more coiled [31]. The effect of increasing salt concentration on thickness is shown in Table 1. Figure 5 highlights the change in linear growth rate with ionic strength. These experiments show that it is possible to tune the thickness of individual bilayers. Elevated linear, and sometimes exponential, trends were also observed in PDDA/PSS, glycosaminoglycans and poly(L-lysine) systems [32, 39, 41-43].

**Table 1.** Average thickness of each bilayer in dependence of sodium chloride concentration [31].

| $C_{NaCl}$ [mol/l] | Average thickness of each bilayer [Å] |
|---|---|
| 0 | 10.0 |
| 1.0 | $17.7 \pm 0.2$ |
| 1.5 | $19.4 \pm 0.3$ |
| 2.0 | $22.6 \pm 0.3$ |
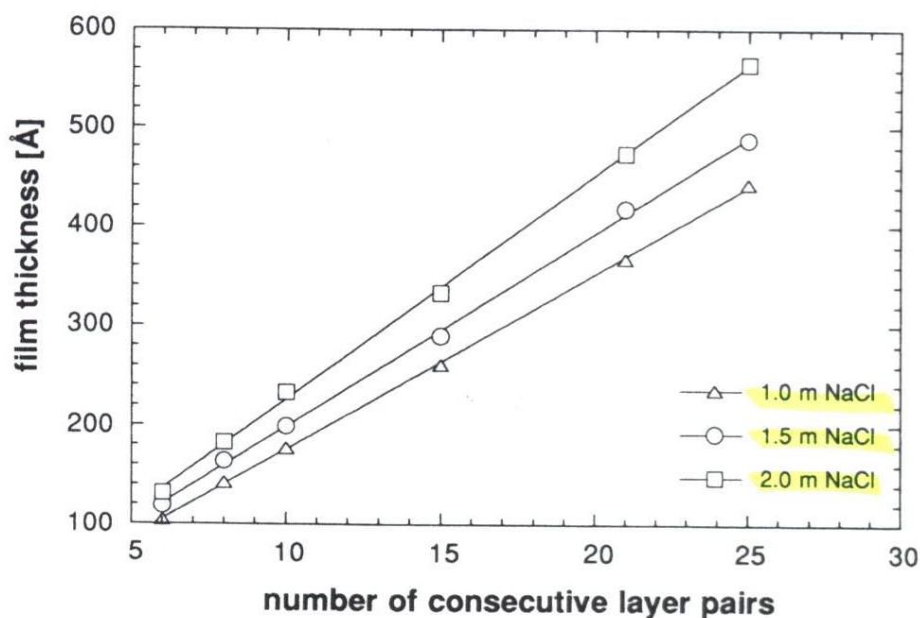


**Figure 5.** Relationship between film thickness and number of bilayers with different concentrations of sodium chloride in the aqueous deposition solution [31].

Increasing salt concentration can change linear growth to exponential growth for the PAH/PSS [37] and PDDA/PSS [12] systems. One explanation for exponential growth deals with the roughness of the film surface [12, 38, 40]. It is clear that film thickness increases with the increase in concentration of added salt. Low salt concentrations exhibit linear growth, and higher concentrations show exponential growth. Some data suggests that thickness has a linear relationship with the square of the ionic strength for different polyelectrolyte pairs [44]. Furthermore, it was found that the deposition thickness of some initial layers at high salt concentrations was not uniform and varies over the first few bilayers before reaching a uniform thickness per bilayer [45]. In a salt free solution, the like charges repel each other, extending the polymer chains. When salt is added, counter ions screen some of the charges allowing the chain to coil more, as shown in Figure 6. Highly coiled polymer chains increase surface roughness as shown in Figure 7. This increased surface roughness contributes to the exponential growth [12], but accumulated roughness can not explain the growth rate at higher bilayers with thickness reaching several micrometers. Elbert and coworkers claim that a complexation process between polyanions and polycations could be the reason for this especially exponential growth [32].
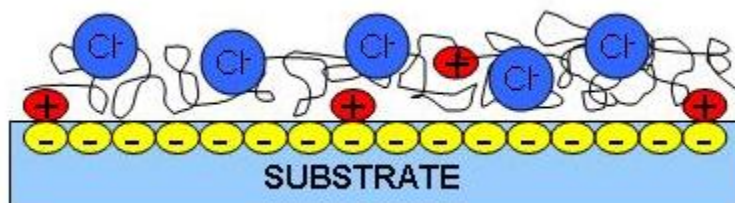


**Figure 6.** Schematic showing how a charge screening increases the film thickness by causing more polymer chain coiling.
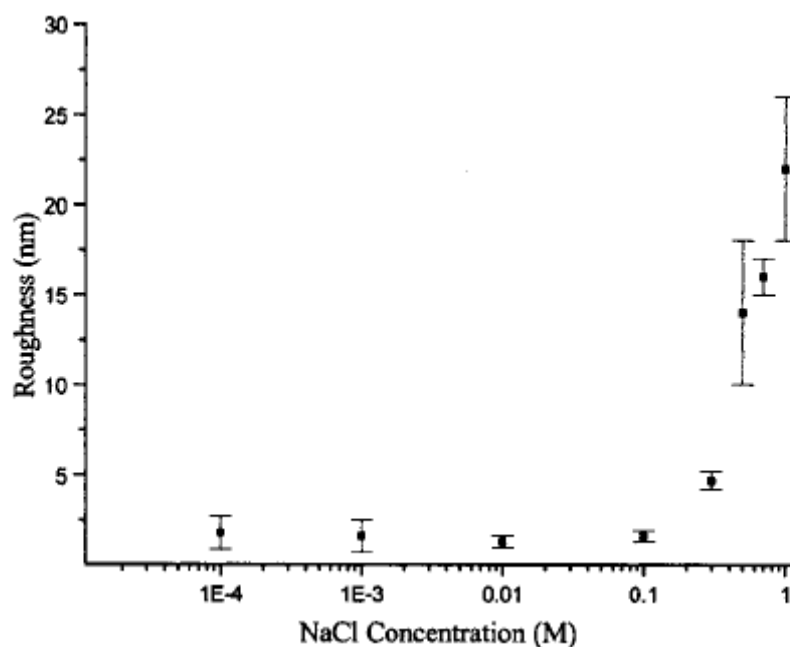
**Figure 7.** The root-mean-square roughness of 10 bilayer films of PDDA/PSS as a function of salt concentration[41].

Exponential growth is most commonly observed when weak polyelectrolytes are used to build assemblies. Weak polyelectrolytes change their charge density in response to a change in pH, which in turn alters the polymer chain confirmation [13, 27]. Rubner and coworkers changed the pH of weak polyanions, such as poly(acrylic acid) (PAA), and weak polycations, such as PAH [13, 27]. In the case of PAA, it is uncharged at low pH and becomes progressively more negatively charged as pH is increased from 3 to 9. PAH exhibits the opposite behavior, becoming more positively charged at low pH. Figure 8 shows the thickness variation of PAH/PAA multilayers controlled by pH of the cationic and anionic dipping solutions.
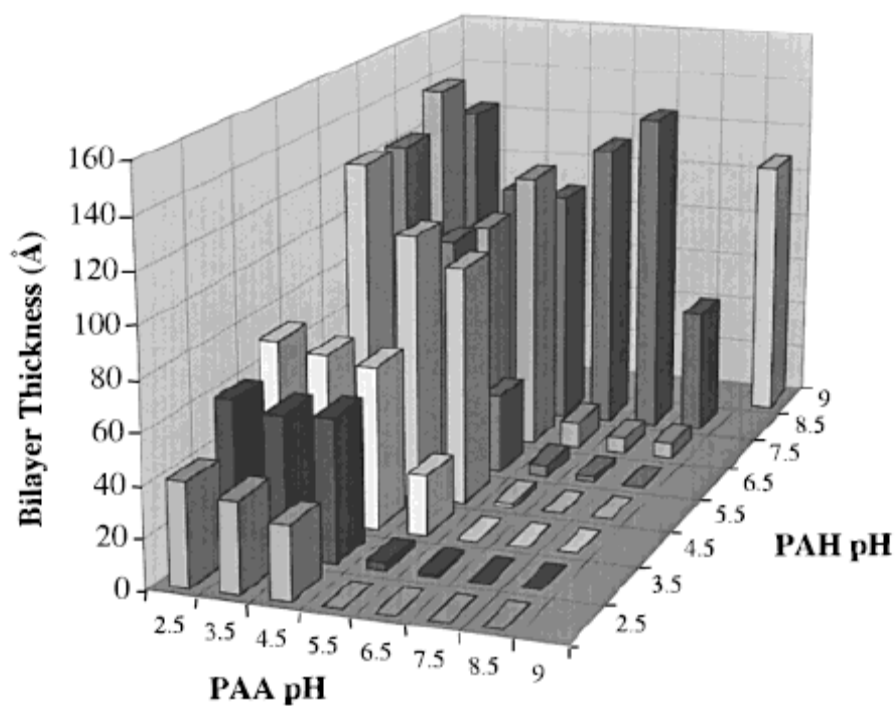
**Figure 8.** Complete matrix of thickness as a function of pH variation of polyelectrolytes [13].

Molecular weight [9, 46], temperature [10, 47], and counter ion [8, 48] are other variables that can alter the thickness of LbL assemblies. For high molecular weight polymers, there is little change in thickness [9], but low molecular weight leads to tight binding and thinner layers [46]. Büscher and coworkers showed that increased deposition solution temperature led to an increase in the thickness of the PAH/PSS system [47]. Van Patten et al. observed a similar temperature effect for poly(diallyldimethylammonium chloride) and poly(styrene sulfonate) [10]. Temperature effects are understood in terms of swelling and melting that alters the electrostatic force between oppositely charged polyelectrolytes. Finally, larger counterions generally produce faster growth due to easier displacement. Barrett and Mermut found that films made with fluoride ($F^-$) as the counterion were 21% thicker after 60s than films made with iodide ($I^-$) as the counter ion

[8]. Better understanding of factors affecting film growth aid the engineering of the functional thin films described below.

2.1.2 Mechanical Properties

Ultra-thin organic films with inorganic nanoparticles have broad applications [49-52]. However, the mechanical properties exhibited by these nanoparticle-filled organic composites are generally worse than predicted [53-61]. The major limiting factors in a composite's mechanical properties are the inability to adequately disperse nanoparticles, the lack of structural control, and the ineffective load transfer from polymer matrix to inorganic nanoparticles [62]. Compared to traditional deposition techniques for inorganic nanoparticle-based ultra thin films, such as sputtering and vacuum evaporation, LbL assembly has several key advantages, including ambient processing conditions, flexibility in substrate size and shape [63], and efficient stress distribution throughout the entire composite [62, 64-65]. In addition to polyelectrolytes, any type of charged particle, including inorganic molecular clusters [66], nanoparticles [67], nanotubes and nanowires [68-69], can be used in a stabilized form for LbL assembly. The addition of inorganic nanoparticles has been shown to increase the mechanical properties of LbL films due to the immobilization of the high strength material inside the polymer matrix [65].

The characterization of mechanical properties for inorganic nanoparticle-based LbL assemblies is complicated by their small physical dimensions. Secondary characterization methods, such as scratch [70], have been used to circumvent this challenge. Advincula and coworkers used nanoindentation to characterize the hardness and elastic modulus of a PDDA/MMT assembly [71]. Measured hardness was 0.46 GPa,

which is higher than typical polymer thin films [71]. Kotov and collaborators made macroscopic freestanding films using LbL assembly and measured the mechanical properties using standard tensile loading [62, 64-65]. Table 2 shows the behavior of films made with PDDA and anionic montmorillonite (MMT) clay [64]. Stress strain curves exhibit similar behavior to that observed in natural nacre [72] and in some bones [73]. Very recently, the Kotov group made a transparent thin film with clay and poly(vinyl alcohol) (PVA) that had a modulus of 100 GPa and tensile strength of 400 MPa [62]. This "plastic steel" [74] is the result of the unique nano brick wall architecture that is only possible with layer-by-layer assembly. Figure 9 highlights the transparency, structure, and stress-strain behavior of these unique films. These types of inorganic-organic assemblies can also have interesting transport properties.

**Table 2.** Mechanical properties of PDDA/MMT films [61].

| Sample type (N) | Tensile strength $\sigma_{UTS}$ (MPa) | Modulus E' (GPa) | Ultimate strain E (%) |
|---|---|---|---|
| PVA (5) | $40 \pm 4$ | $1.7 \pm 0.2$ | $35 \pm 4$ |
| PVA with GA (5) | $40 \pm 10$ | $2.0 \pm 0.5$ | $3.3 \pm 1.3$ |
| PDDA (5) | $12 \pm 4$ | $0.2 \pm 0.03$ | $48 \pm 9$ |
| PDDA-MMT (*) | $100 \pm 10$ | $11 \pm 2$ | $10 \pm 2$ |
| PVA/MMT | $150 \pm 40$ | $13 \pm 2$ | $0.7 \pm 0.2$ |
| PVA/MMT with GA (5) | $400 \pm 40$ | $106 \pm 11$ | $0.33 \pm 0.04$ |

* Data are the previously published results by Tang *et. al* [49] for 1.2-to-4.9-μm-thick (50 to 200 bilayers) samples tested at relative humidity of 32%.
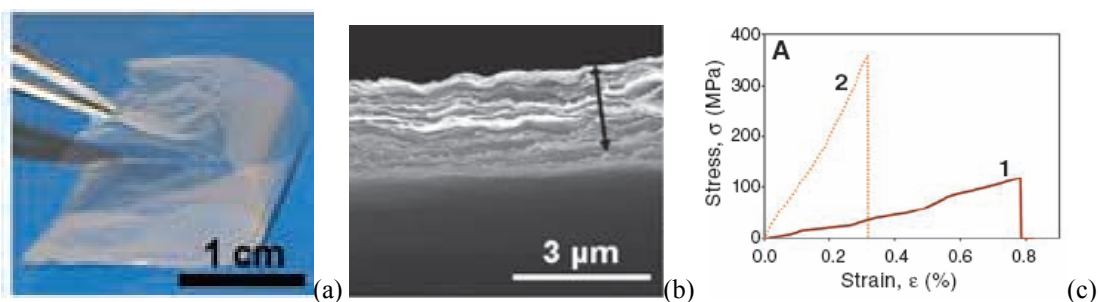


**Figure 9.** 300-bilayer PVA/MMT free-standing film (a), SEM cross sectional image (b), and stress strain curves (c) [62]. Curve 1 has no cross-linking and curve 2 is cross-linked.

2.1.3 Transport Properties

For the past two decades, the demand for flexible displays and smart windows has been steadily increasing [75-77]. One technology used in flexible dislays is electrochromism (i.e., color change with applied electric field). Electrochromics are of interest due to their low cost and reasonable contrast in a variety of colors [78-80]. Current electrochromic research is focused primarily on thin polymer films [79]. Competing technologies are liquid crystal displays (LCDs) and organic light emmiting diodes (OLED) [81-82]. Conventional techniques for producing electrochromic polymer films are electropolymerization and spin-casting with soluble derivatives [82]. Layer-by-layer assembly has several advantages over these techniques, such as simplicity, low cost, and the ability to mix various functional materials in a single film without phase separation [82]. Hammond and coworkers created a dual electrochrome composite via LbL [81]. Here both the polycation and polyanion were cathodically coloring electrochromic species. Poly(hexylviologen) (PXV) was the polycation and PEDOT-PSS was the polyanion. In other variations, Hammond and coworkers used polyaniline (PANI) and poly(2-acrylamido-methane-2-propanesulfonic acid) (PAMPS) as polycations with anionic PEDOT-PSS [82]. Figure 10 shows the UV/Vis spectral behavior for 20 bilayers of LPEI/PEDOT-PSS and PANI/PAMPS films with varying levels of oxidation/reduction. Strong absorption of the reduced LPEI/PEDOT-PSS system occurs at 654nm, while oxidation shifts the absorption band from a neutral peak to a new peak at 860nm. A variety of other researchers have also studied electrochromic assemblies [83-85], with Grunlan et al. achieving a contrast ratio greater than 10 with tungstate ($WO_4^{2-}$) as the anion [86].
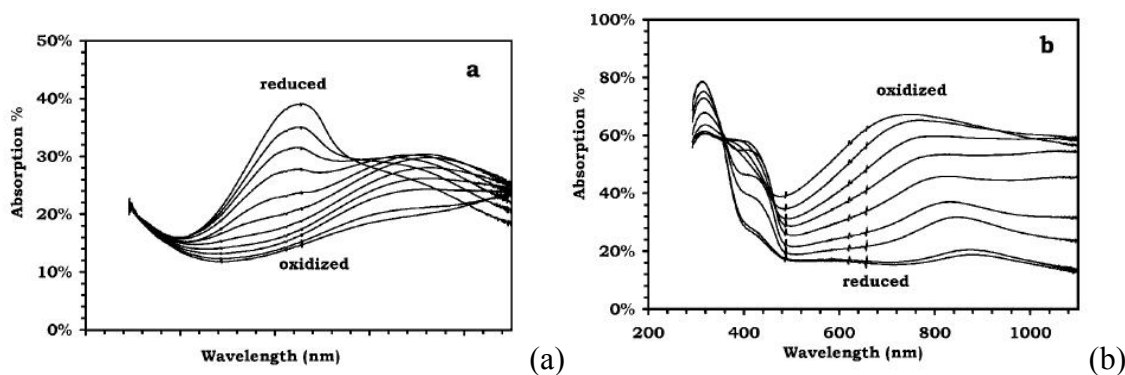
**Figure 10.** UV/Vis adsorption of 20 bilayers of LPEI/ PEDOT:PSS (a) and PANI/PAMPS (b) [82].

Purely electrically conductive thin films were also produced using LbL assembly in conjunction with carbon black (CB) [87], PEDOT-PSS [88], carbon nanotubes [89] and colloidal gold [70]. Carbon black (CB) has been used extensively to create electrically conductive polymer composites. Conventional techniques to make carbon black-based composites are melt mixing [71-93] and solution processing [94-95]. In these techniques, a significant concentration of carbon black (25 wt%) is required to generate sufficient levels of electrical conductivity. This high concentration of carbon black causes problems, such as high mixing viscosity, brittle mechanical behavior, and high porosity due to aggregation [96-97]. The LbL process overcomes these problems by using dilute mixtures (< 1wt% solids). Grunlan and coworkers created films with tunable electrical conductivity and transparency using LbL deposition of CB stabilized with polyethyleneimine (PEI) and poly(acrylic acid) (PAA) [87]. Figure 11 shows how sheet resistance ($R_S$) decreases and thickness increases as a function of the bilayers deposited. Films with bulk resistivity below 0.3 $\Omega \cdot$cm were produced, which is much lower than traditional CB- filled composites [98]. Resistivities below 0.01 $\Omega \cdot$cm were achieved by others using carbon nanotubes [89] or colloidal gold [90].
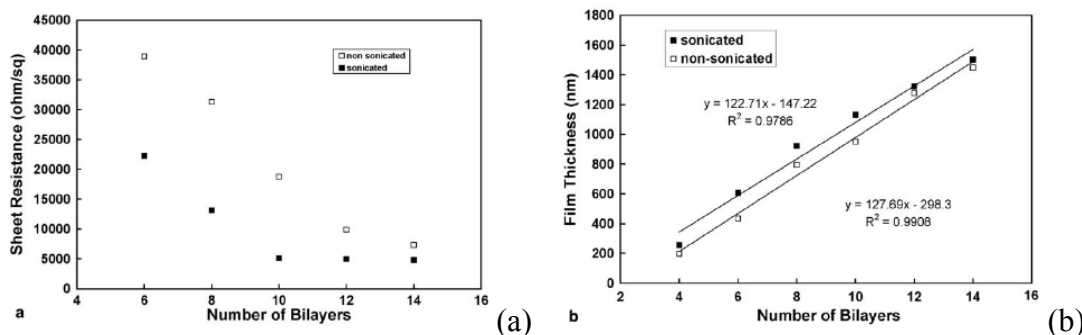
**Figure 11.** Sheet resistance (a) and film thickness (b) as a function of the number of carbon black-filled bilayers deposited. The behavior of films made with and without sonication of deposition mixtures are compared [87].

Much like for electrical conductivity, layer-by-layer deposition offers several advantages for making ionically conductive thin films. These films have flexibility with mechanical properties superior to gels and crystalline solids, thin and defect free surfaces, and uniform deposition on nonplanar surfaces [99]. An early ion conduction study of the effects of temperature, pH, and moisture on LbL assemblies was performed by Durstock and Rubner [100]. Maximum ion conductivity at room temperature and high humidity is $2 \times 10^{-7}$ S/cm [100], which is too low to be practical for most electrochemical applications. Hammond and coworkers maximized the small ion concentration and minimized the cross-link density to achieve higher ion conductivity [99]. They used linear polyethylenimine (LPEI) as a cationic polyelectrolyte and Nafion, PAMPS, and PAA were used as anionic polyelectrolytes. The impedance spectroscopy of real and imaginary values was fitted by a simple equivalent circuit shown in Table 3. The most recent assemblies designed for ion conduction can achieve $9 \times 10^{-10}$ S/cm for neat PEO/PAA assemblies [101].

**Table 3.** Ionic conductivity data for LbL assemblies at room temperature (25°C) [99].

| | ionic conductivity (S/cm) | | | |
|---|---|---|---|---|
| system | 17% RH | 52% RH | 100% RH | wet |
| (LPEI/NAFION)$_{30}$ no salt | $5.0 \pm 1.5 \cdot 10^{-11}$ | $3.4 \pm 0.4 \cdot 10^{-11}$ | $2.9 \pm 0.1 \cdot 10^{-9}$ | $4.8 \pm 0.1 \cdot 10^{-9}$ |
| (LPEI/NAFION)$_{30}$ 0.1 M NaCl | $1.2 \pm 0.2 \cdot 10^{-11}$ | $8.3 \pm 0.4 \cdot 10^{-11}$ | $6.9 \pm 0.4 \cdot 10^{-9}$ | $3.8 \pm 0.3 \cdot 10^{-9}$ |
| (LPEI/PAMPS)$_{30}$ no salt | $1.5 \pm 0.5 \cdot 10^{-9}$ | $9.4 \pm 0.7 \cdot 10^{-6}$ | $1.0 \pm 0.1 \cdot 10^{-5}$ | delaminated |
| (LPEI/PAMPS)$_{30}$ 0.2 M NaCl | $2.7 \pm 0.4 \cdot 10^{-12}$ | $1.3 \pm 0.0 \cdot 10^{-8}$ | $1.5 \pm 0.2 \cdot 10^{-5}$ | delaminated |
| (LPEI/PAA)$_{30}$ pH 2 | $6.7 \pm 0.3 \cdot 10^{-12}$ | $5.6 \pm 0.6 \cdot 10^{-10}$ | $1.2 \pm 0.1 \cdot 10^{-6}$ | $9.7 \pm 0.8 \cdot 10^{-7}$ |
| (LPEI/PAA)$_{30}$ pH 5 | $2.8 \pm 0.2 \cdot 10^{-11}$ | $6.4 \pm 0.2 \cdot 10^{-9}$ | $1.0 \pm 0.0 \cdot 10^{-5}$ | $5.8 \pm 0.2 \cdot 10^{-6}$ |

A variety of other transport behaviors of LbL assemblies have been studied. By coating drug-containing micro particles with the LbL process, drug release can be prolonged and controlled [102-103]. Delivering drugs through the skin has several advantages over pills and injections, such as decreased liver damage [104], steady blood level profile [105], patient compliance [106], and avoiding first pass metabolism [107]. Even with these advantages, a suitable drug reservoir capable of stabilizing and accurately delivering high molecular weight (>500g/mol) and/or hydrophilic molecules is a critical hurdle to overcome. LbL assembly is also capable of acting as a transdermal drug reservoir [108]. Finally, assemblies of poly(allylamine hydrochloride), poly(acrylic acid) (PAA), and saponite clay produced a 60% reduction in PET permeability with ten PAH/PAA/PAH/seponite quad-layers [109]. Clay-polyacrylamide assemblies (described in Chapter IV) have achieved more than 1000 times reduction of 7-mil PET with 30-bilayers [110].

## 2.2 Barrier Films

2.2.1 Tortuous Path Theories

Inorganic nanoparticles can block the diffusion of gases or liquids in a permeable (e.g., polymeric) matrix. If the inorganic nanoparticles are impermeable, then the

diffusing molecules have to go around them. This assumption leads us to the tortuous pathway theory. Equation 1 is an initial approximation:

$$P_F / P_U = \phi_P / \tau \tag{1}$$

where $P_F$ and $P_U$ are permeability of the filled and unfilled polymer, respectively, $\phi_P$ is the volume fraction of the polymer [111-115], and $\tau$ is the tortuous factor which is the distance a molecule must travel to get through the film divided by film thickness. A required assumption is that the fractional area occupied by the polymer in any cross section is equal to the volume fraction of the polymer. Permeability is independent of thickness, which means $P_F/P_U$ is not proportional to thickness.

Nielsen created the formal tortuosity theory [15]:

$$\tau = 1 + (L/2W)\phi_F \tag{2}$$

where L is the length of a face of a filler particle, W is the thickness of filler plates, and $\phi_F$ is the volume fraction of filler. A large aspect ratio (L/W) produces decreased permeability if the particle lies with its largest dimension parallel to the substrate surface. Figure 12 shows an illustration depicting a tortuous path.
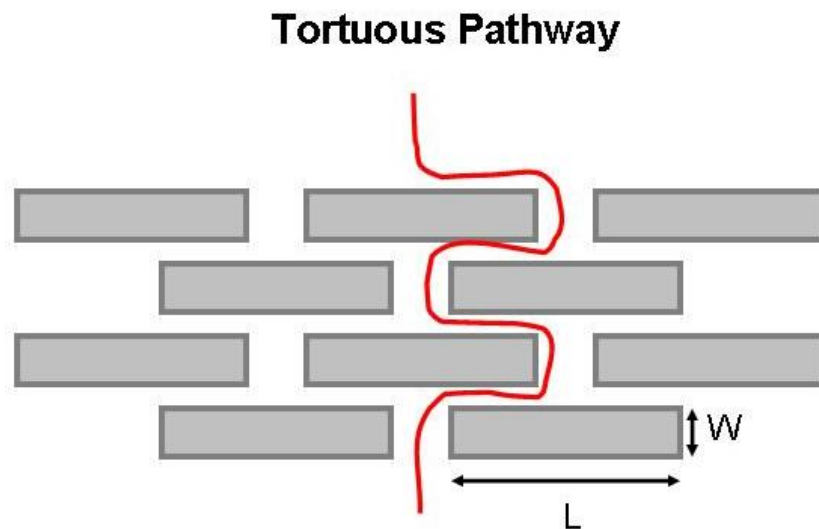


**Figure 12.** Path of diffusing molecule through a tortuous pathway of impermeable particles.

Maxwell originally proposed a model for the diffusion coefficient of a periodically arrayed impermeable sphere-filled matrix [116], and Raleigh proposed a diffusion coefficient model for periodically arrayed infinite cylinders oriented parallel to the membrane surface [117]. Cussler and coworkers later proposed an advanced tortuous path theory as an extension of Nielson's concept [118]. They considered the two idealized cases consisting of regularly distributed slits and pores. Based on these ideal cases, they built Equation 3, which can explain the diffusion flux through randomly distributed impermeable flakes in a polymer matrix:

$$J_N = \frac{J_0}{1 + \mu\alpha^2\left[\phi^2/(1-\phi)\right]} \tag{3}$$

where $J_0$ is total flux, $J_N$ is the flux across a membrane with N flakes, $\mu$ is the combined geometric factor, $\alpha$ is the flake aspect ratio, and $\phi$ is the volume fraction of flakes. The geometric factor is related to flake shape and will be explained in more detail later in this section. Figure 13 shows schematics of a realistic case (a), regularly placed slits (b), regularly placed pores (c), and randomly placed slits (d). The assumption of Equation 3 is randomly sized rectangles that are randomly located in the discrete planes.
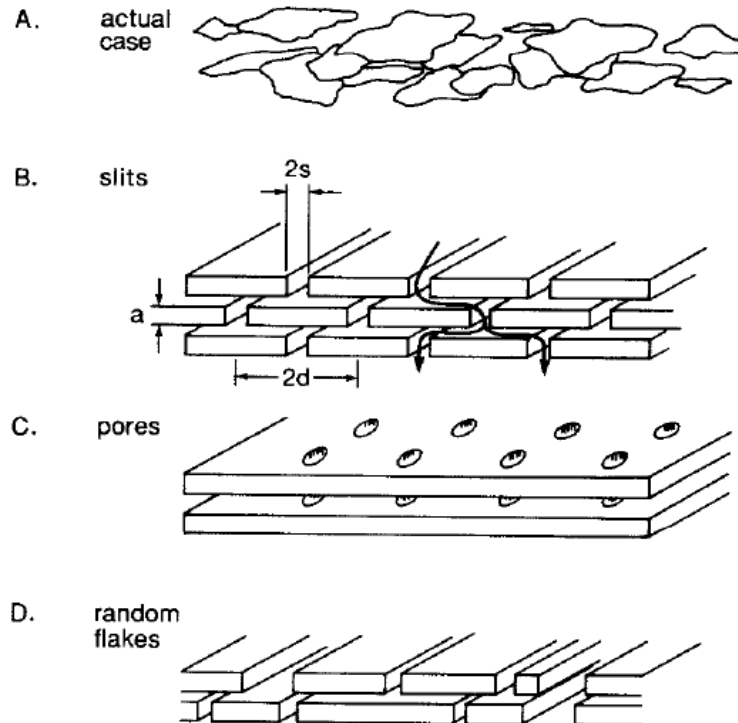
**Figure 13.** Schematics of an actual membrane (A), diffusion through slits (B), diffusion through pores (C), and diffusion through randomly spaced slits or pores (D) [118].

Equation 4 is Cussler's model for diffusion coefficient [118]:

$$D = \frac{D_0}{1 + \alpha^2 \phi^2 / (1 - \phi)} \quad (4)$$

where $D_0$ is the diffusion coefficient without impermeable flakes, D is the composite diffusion coefficient, $\alpha$ is the flake aspect ratio, and $\phi$ is the volume fraction of impermeable flakes. Equation 4 has been verified experimentally [116, 18-19, 119-120] and through Monte Carlo simulations [120]. The second term in the denominator of Equation 4 is the resistance to diffusion of the tortuous path around the flakes, known as a "wiggle." The square of $\alpha$ and $\phi$ reflects the increased diffusion distance and the reduced cross-sectional area between the flakes. This wiggling is the most important factor of the increased resistance in flake-filled barrier membranes [116, 18-19, 119-120].

Cussler and coworkers later improved their own model, shown schematically in Figure 14, which takes into account the resistance to diffusion of the slits between adjacent flakes in the same horizontal plane and the constriction of the solute to pass into and out of the narrow slits [121]. Equation 5 represents this model:

$$\frac{D_0}{D} = 1 + \frac{\alpha^2 \phi^2}{1-\phi} + \frac{\alpha\phi}{\sigma} + \frac{4}{\pi} \cdot \frac{\sigma\phi}{1-\phi} \cdot \ln\left[\frac{\pi\alpha^2\phi}{\sigma(1-\phi)}\right] \qquad (5)$$

where $\sigma(=s/a)$ is the slit size. The third term on the right hand side, $\alpha\phi/\sigma$, is the resistance to diffusion of the slits between adjacent flakes in the same horizontal plane and the fourth term on the right hand side is the constriction of the solute when passing into and out of the narrow slits. In the current work, $\alpha$ and $\phi$ were empirically determined to fit the experimental data, as seen in Chapter IV.
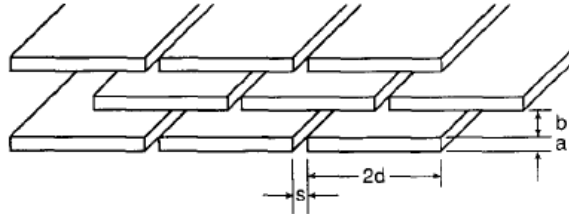


**Figure 14.** Schematic of Cussler's improved diffusion coefficient model [19].

By combining the diffusion flux and diffusion coefficient models, Cussler and coworkers were able to determine the permeability of flake aligned composite coatings [122] and polydispersed flake-based barrier films [123]. When $\phi<<1$ and $\alpha\phi<1$, the permeability of the composite is [15]:

$$P = \frac{P_0}{1+\alpha\phi} \qquad (6)$$

However, when $\phi<<1$ and $\alpha\phi>1$, the permeability of the composite becomes [116, 20]:

$$P = \frac{P_0}{1 + \mu \alpha^2 \phi^2 / (1 - \phi)} \tag{7}$$

There are several conditions to consider for the geometric parameter. If the flakes are periodic, well aligned, ribbon-like, and their length is greater than their width, the geometric factor is 1. If the ribbon-like flakes are misaligned, a wiggle or tortuous path is unachievable. Since the alignment and misalignment occur with equal probability, the geometric factor is 0.5. Figure 15 depicts these two extreme cases. If the flakes are hexagonal and periodic, then the geometric factor is 4/9. If the flakes are randomly distributed and hexagonal, then the geometric factor is 2/27. Since the flakes' shape cannot be perfectly uniform ribbon-like or hexagonal, the experimental geometric factor should lie between 2/27 and 1/2.



(a)                                                                    (b)
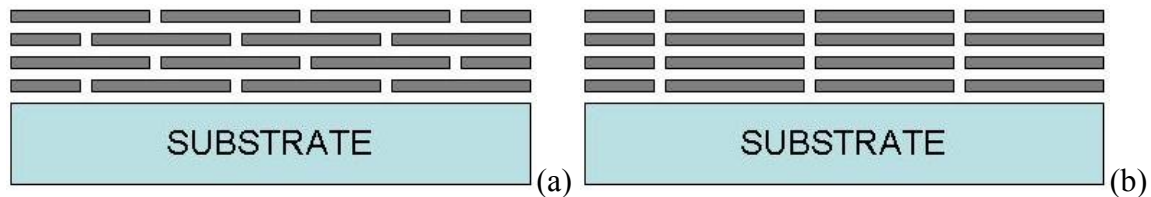
**Figure 15.** Well-aligned flakes (a) and misaligned flakes (b).

Fredrickson et al. developed a barrier model that includes several additional assumptions [21]: the matrix is homogeneously filled with impermeable flakes, the flakes are disks and the directional vector of the flake surface is parallel to the diffusion direction. Equation 8 represents this model:

$$\mathbf{D} = D_{\parallel} \mathbf{\hat{u}}\mathbf{\hat{u}} + D_{\perp}(\delta - \mathbf{\hat{u}}\mathbf{\hat{u}}) \tag{8}$$

where $\mathbf{D}$ is the diffusion tensor and $\mathbf{\hat{u}}$ is a directional vector of the flake surface. $D_{\parallel}$ and $D_{\perp}$ denote diffusion coefficients parallel and perpendicular to $\mathbf{\hat{u}}$ and $\delta$ is the unit tensor.

When the flakes have a very small aspect ratio and perfect alignment, $D\perp$ is the same as $D_0$ (the diffusion coefficient of the neat matrix). The final assumption is that diffusivity in the matrix is independent of the presence of particles. Fredrickson et al. also defined the dilute regime and semidilute regime, where $\phi<<1$ and $\phi R/(2\pi a)<<1$, is a dilute regime, and $\phi<<1$ and $\phi R/(2\pi a)>1$, is the semi-dilute regime. Figure 16 depicts these regimes, where R is the radius and 2a is the thickness of the impermeable disk.
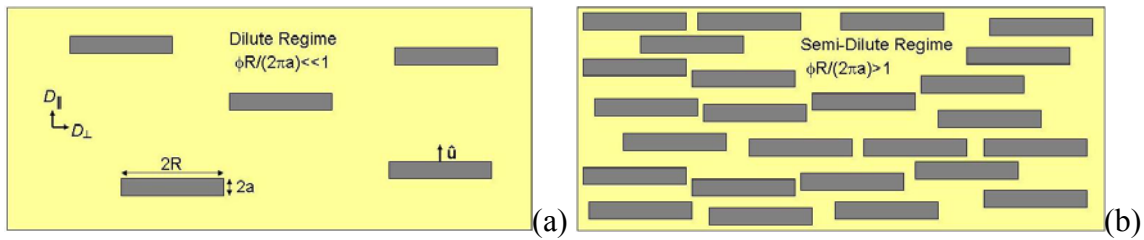


**Figure 16.** Dilute regime (a) and semi-dilute regime (b) for Fredrickson's model.

The governing equation of the dilute regime is:

$$\frac{P}{P_0} = 1 - \frac{\pi}{\ln\alpha}(\alpha\phi) + O\left[(\alpha\phi)^2\right] \qquad (9)$$

where $\alpha(=R/2a)$ is the aspect ratio of the disk. This equation can be repsented by a series expression:

$$\frac{P}{P_0} = 1 - \kappa(\alpha\phi) + \kappa^2(\alpha\phi)^2 + O\left[(\alpha\phi)^3\right] \qquad (10)$$

which can be rewritten as:

$$P = \frac{P_0}{1 + \kappa(\alpha\phi)} \qquad (11)$$

where $\kappa$ is geometric factor $(=\pi/\ln\alpha)$. Unlike Fredrickson's model, Cussler's model for the dilute regime does not have a geometric factor.

Fredrickson modified the geometric factor for the semi-dilute regime from Cussler's model [116, 20]. Fredrickson's geometric factor for semi-dilute regime is:

$$\mu = \frac{\pi^2}{16\ln^2 \alpha}$$

(12)

The critical difference between Cussler's model and Fredrickson's model is the shape of impermeable flakes creating a difference in geometric factors. If the flakes are polydispersed in size, then the geometric factor has little influence [123]. These tortuous path theories have laid the groundwork for the current understanding of platelet filled polymer composites used in barrier applications.

## 2.2.2 Filled Polymers

Inorganic nanoparticle–filled polymer composites have relatively low density, improved barrier properties, and enhanced mechanical properties [124]. In addition to these benefits, inorganic nanoparticle–filled polymer composites have recently been shown to exhibit excellent flame retardant behavior [125, 126]. Adding impermeable inorganic nanoparticles to bulk polymer films is a common route to reduce oxygen transmission rate (OTR) [127-140]. Clay platelets are especially effective for gas barrier due to their nano thickness (~1nm) and large aspect ratio (10 < l/d < 2000, depending on type). Giannelis and coworkers have extensively studied the synthesis and characterization of impermeable nanoparticle-filled oxygen and moisture barrier films [124-125, 126]. They used melt intercalation of polymer [141], which can be applied to a non-polar polymer matrix, such as polystyrene, or to a strongly polar polymer matrix, such as nylon [126]. An intercalated structure has a single polymer chain in between the

silicate layers, in the case of clay platelets. Disordered systems have exfoliated and dispersed silicate layers in the polymer matrix, as shown schematically in Figure 17.
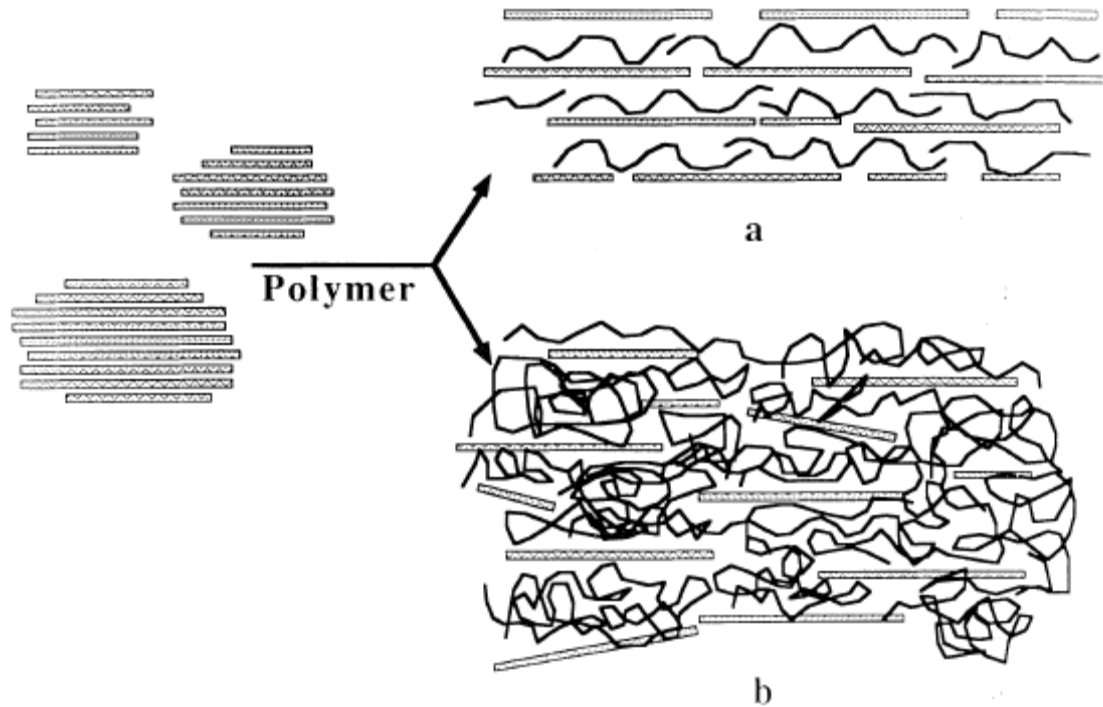


**Figure 17.** Layered silicates-filled polymer composites can have an intercalated (a) or disordered structure (b) [135].

Montmorillonite layered silicates (MLS) are ceramic platelets with a high aspect ratio [137], typically >100nm in diameter and 1nm thick. This high aspect ratio creates a tortuous path for gas molecules moving through the polymer matrix, which creates a large diffusion length that lowers the permeability [14-15]. Unlike SiOx films and polymer multilayer films (see section 2.2.3), clay-filled polymer composites typically suffer from poor transparency and relatively high OTR [107]. Figure 18 shows how a typical composite's barrier is reduced by the addition of clay. Most systems show an OTR or permeability reduction of 1 to 100% [126, 128-129, 138-139], but a few show an order of magnitude improvement [142].
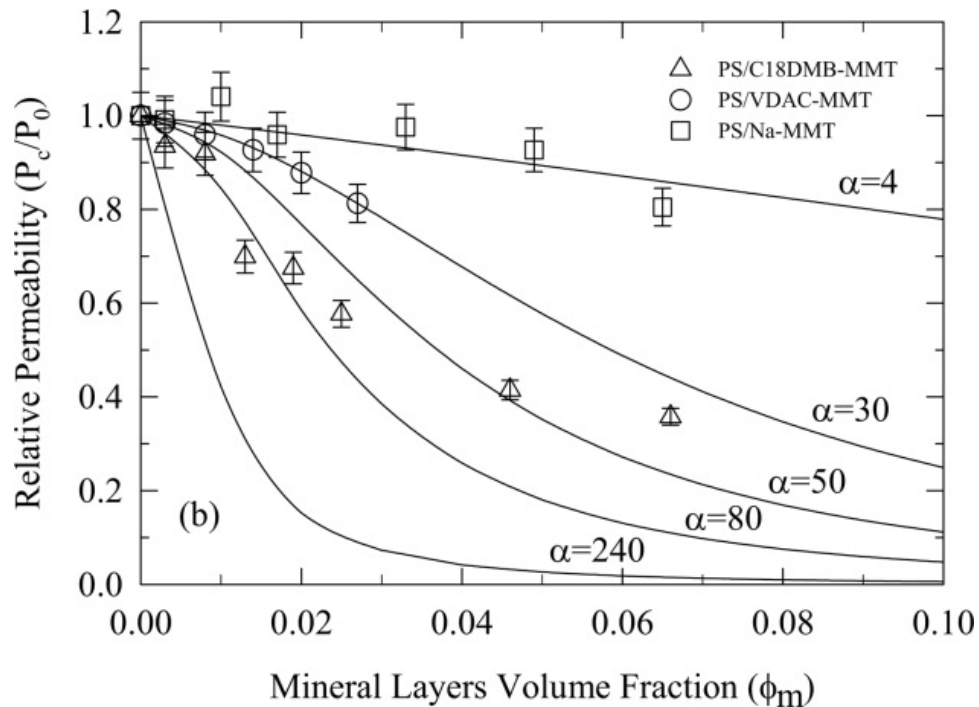
**Figure 18.** Experimental data of relative permeability $P_c/P_0$ versus volume fraction of mineral layers $\phi_m$ with various fits using Equation 7 [142].

### 2.2.3 Ceramic Barriers

Silicon oxide (SiOx) films are widely used as barriers due to their low OTR, high transparency, and microwaveability [143-146]. Barrier coatings for food and medical applications must exhibit low oxygen and moisture diffusion [147]. These SiOx barriers are relatively thin and this enhances their transparency. SiOx coatings are produced using plasma-enhanced chemical vapor deposition (PECVD) [148-149]. Despite being a relatively mature technology, SiOx coatings suffer from a variety of problems that include cracking and poor adhesion to plastic substrates [150-151]. Additionally, PECVD is an involved process that increases the manufacturing cost of a barrier film.

Polymer multi-layer (PML) is a more recent technology that uses conventional sputtering to build an alternating polymer/ceramic multilayer [152]. The thickness of each layer is an order of magnitude thicker than that deposited using LbL deposition.

PML films were developed as a packaging solution for a variety of electronics applications (e.g., organic light emitting diodes and photovoltaic cells) [153-155]. These films are more flexible than traditional SiOx, but the processing is very involved and the ceramic layers are still prone to cracking. Table 4 and Figure 19 compare the characteristics of clay-filled polymer composites, SiOx-coated substrates, and the PML system. In general, the ceramic barriers (SiOx and PML) have much better barrier, but less flexibility, than clay-filled polymers. Layer-by-layer assembly of polymer and clay offers the ability to combine the best attributes of all these systems [107].
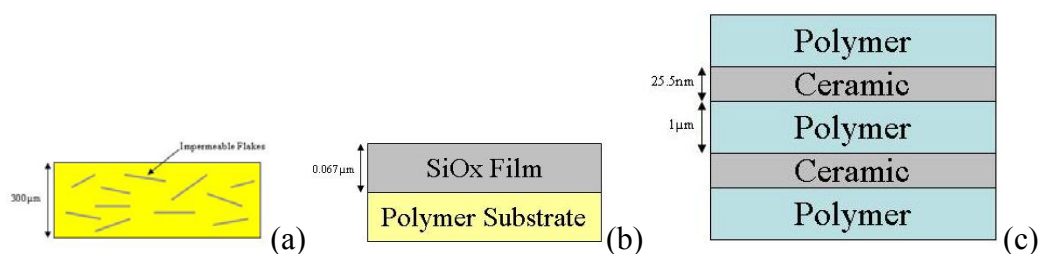
**Figure 19.** Schematics of a bulk inorganic-filled composite (a), SiOx barrier film (b) and polymer multi-layer (c).

**Table 4.** Oxygen transmission data for the most common barrier technologies.

| | SiO$_x$[a] | | | PML[b] | | Nanocomposite[c] | |
|---|---|---|---|---|---|---|---|
| | Bare | Coated | Coating | Bare | Coated | neat | Clay-Filled |
| Thickness (μm) | 12 | 12.067 | 0.067 | 50 | 51 | 175 | 175 |
| OTR (cc/m$^2$/day/atm) | 127.6 | 3.081 | 3.143 | 30.55 | <<0.0155 | 28.50 | 7.993 |
| Permeability ($10^{-6}$ cc/m/day/atm) | 1532 | 37.17 | 0.2105 | 1528 | <<0.791 | 8552 | 2398 |

[a] Measurements were made with an OXTRAN instrument (Mocon, Minneapolis, MN), at 30°C and 70% RH. [156]
[b] Measurements were made with an OXTRAN instrument (Mocon, Minneapolis, MN) [152]
[c] Measurements were made with a GDP-C Permeability Tester (Muenchen, Germany), according to ASTM 1434-82. PET was melt-processed with 5% MMT [157].

# CHAPTER III

# ROBOTIC DIPPING SYSTEM

## 3.1 Introduction

Many of the functional thin films made using layer-by-layer assembly (see examples in Chapter II) require more than ten bilayers, or twenty total dipping cycles, to achieve a desired property. With many systems requiring dip times of five minutes or more, this process is too time consuming and prone to human error to be done by hand. Several research groups have used a modified slide stainer [158-160], while others use some form of home-built [45, 161] or commercially-built robot [162-164] to automate this process of repetitive dipping. These automated systems are capable of producing tens of bilayers in a reproducible manner without constant supervision. Despite the widespread use of customized robotic equipment for layer-by-layer assembly of thin films, little detail on the robot itself has been published in these reports. A simple, but very flexible robotic system was developed for this project [165] and is described in detail below.

## 3.2 Experimental

### 3.2.1 Robot Design

The robotic system is composed of an aluminum frame, three linear, screw-driven actuators, solution cells, rinsing and drying stations, controller and relay, drain reservoir, and computer controller. Figure 20 is a schematic diagram of the frame and three BiSlide assemblies from Velmex, Inc. (Bloomfield, NY), which were connected to produce three-

dimensional positioning. Each axis is driven by its own stepper motor. The X axis holder

is stationary (i.e., attached to the frame) and its moving part holds the Y axis, while the

moving part of Y-axis holds the Z axis that holds the sample. The X, Y, and Z axes have

a movement range of 38, 33, and 33 inches, respectively. Each stepper motor has a

resolution of 0.00025" per step and operates at a maximum speed of 6000 steps per

second (1.5"/s).
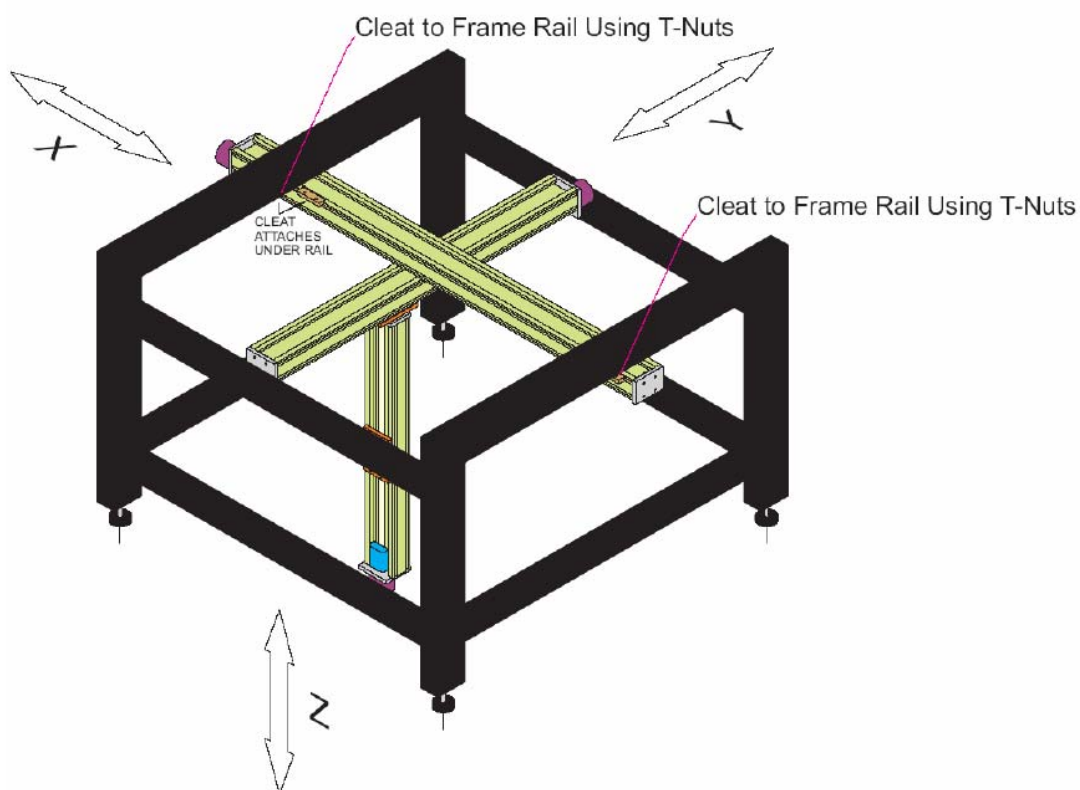


**Figure 20.** Schematic of frame and linear actuators used to produce three-dimensional motion (picture courtesy of Velmex, Inc.).

Figure 21 shows the actual robot with the key parts labeled. The two groups of 12

6x6" cells mark the locations where aqueous solutions or mixtures can be placed. In a

typical deposition, the left side cells contain positively-charged materials and the right

side cells contain negatively-charged materials. The rinsing and drying stations are in the center to avoid cross-contamination between oppositely charged mixtures. Neighboring cells are not occupied to further avoid cross-contamination amongst liquids, allowing a maximum of 12 different ingredients for deposition in a single preparation with the current configuration.



**Figure 21.** Image of robotic dipper built for LbL assembly.

The central section of the platform sprays the sample with water that is immediately drained away, decreasing the likelihood of contamination and swelling of the film between depositions. Rinsing is accomplished with a 12 volt DC gear pump, Model PQ-DC from Greylor (Coral Gables, FL), that supplies deionized water from a 50-L reservoir. The Greylor pump has plastic gears that eliminate the possibility of metal ion

contamination that would be associated with metal gears. House air is then used to dry the sample, but this line can be easily attached to any gas source to accommodate alternate requirements. A heavy duty two-stage filter from McMaster-Carr (Chicago, IL) is attached between the air nozzle in the wall and the drying station to eliminate water and oil-based impurities. Rinsing and drying times are controlled by the speed with which the sample is raised between the spray nozzles. Water is conserved by running the pump only when the sample is between the rinsing nozzles. Most of the robotic systems currently used to produce LbL assemblies immerse the sample in water as a means of rinsing [158-164].

3.2.2 Robot Operation

The robot is controlled with LabVIEW 7.1 software from National Instruments (Austin, TX). LabVIEW code controls the three stepper motors and one relay using VISA communication. Figure 22 shows the input screen that is used to generate a dipping program. The manual command mode initializes the stepper motors and relay. In other words, motor speed and initial position are put into the 'Manual Input' box prior to setting up the actual dipping program. Automatic mode is then selected to choose the number of dipping cycles and the time for each dip. Automatic mode is composed of a case structure with two sequential structures, where the first sequential structure is the initial dipping and next sequential structure is the continual dipping cycle. Only the white boxes are used for programming, while the grey boxes are pre-determined or filled in as the dipping program is executed. The screen shown in Figure 22 allows four mixtures to

be used to allow bilayers of one composition to be followed by bilayers of a completely different composition. In this way nano-scale 'stripes' could be produced.
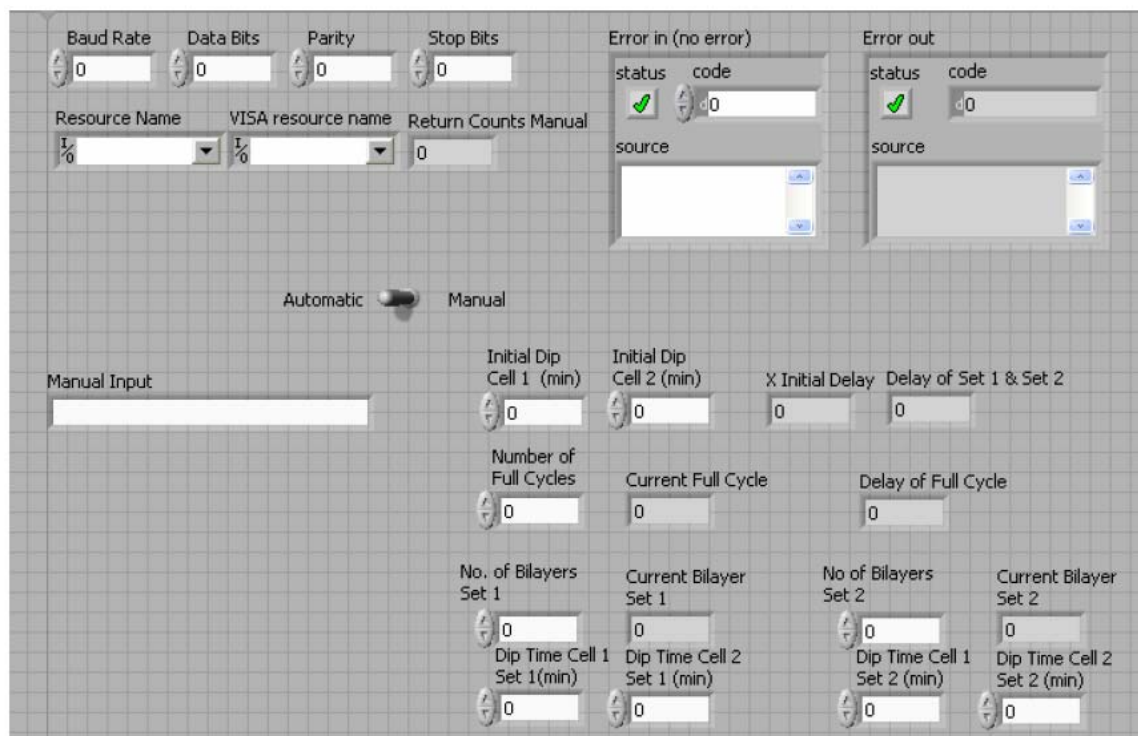


**Figure 22.** Programming screen for the robotic dipper. The user can choose how many bilayers of each system should be deposited for each of two sets of ingredients. Immersion time in each mixture can also be specified in minutes. The software will keep track of how many bilayers have already been deposited [165].

3.2.3 Materials

Cationic polyacrylamide (PAm) (tradename Superfloc C-491) was provided by CYTEC (West Paterson NJ). This is a copolymer containing 5 mol % of positively-charged repeat units. Southern Clay Products, Inc. (Gonzales, TX) supplied natural, untreated montmorillonite (MMT) (tradename Cloisite $NA^+$). This clay has a cationic exchange capacity of 0.926meq/g and is negatively-charged in deionized water. MMT platelets have a density 2.86 $g/cm^3$, diameter of 10~1000nm, and thickness of 1nm [166]. Poly(acrylic acid) (PAA) and polyethylenimine (PEI) were purchased from Aldrich

(Milwaukee, WI). PEI is a weak polycation with a molecular weight of 25,000 g/mol, while PAA is a weak polyanion with a molecular weight of 100,000 g/mol. Both polymers were used as supplied without further purification or alteration. Poly(ethylene terephthalate) (PET) film (tradename Melinex ST505), with a thickness of 175 µm, was purchased from Tekra Corporation (New Berlin, WI) and used as the substrate in this study. Conductex 975 Ultra carbon black (CB) was supplied by Columbian Chemical (Marietta, GA). This grade of CB has a nitrogen surface area (NSA) of 242 $m^2$/g and a primary particle size of 21 nm. Single side polished (100) silicon wafer (University Wafer, South Boston, MA) acted as the substrate for thickness measurements made with an ellipsometer.

**3.3 Results and Discussion**

Figure 23 compares the thickness of hand-dipped films and robot-made films. Films were deposited onto silicon wafers using aqueous mixtures containing 0.2 wt.% MMT (anionic clay) and 0.25 wt.% cationic polyacrylamide. These clay-filled assemblies are completely transparent, so thickness was measured using a PHE-101 Discrete Wavelength Ellipsometer made by Microphotonics (Allentown, PA). There were five hand dipped and three robot dipped samples tested at each number of bilayers. The error bars represent one standard deviation. An analysis of variance (ANOVA) (see Appendix A) [167] was conducted, with the results indicating that the thickness differences up to 25 bilayers are insignificant between the two deposition methods. ANOVA results for the 30-bilayer sample suggest that the thickness from hand dipping and robotic dipping do

have a significant difference. What appears to be exponential growth for this system will
be examined more closely in Chapter IV.
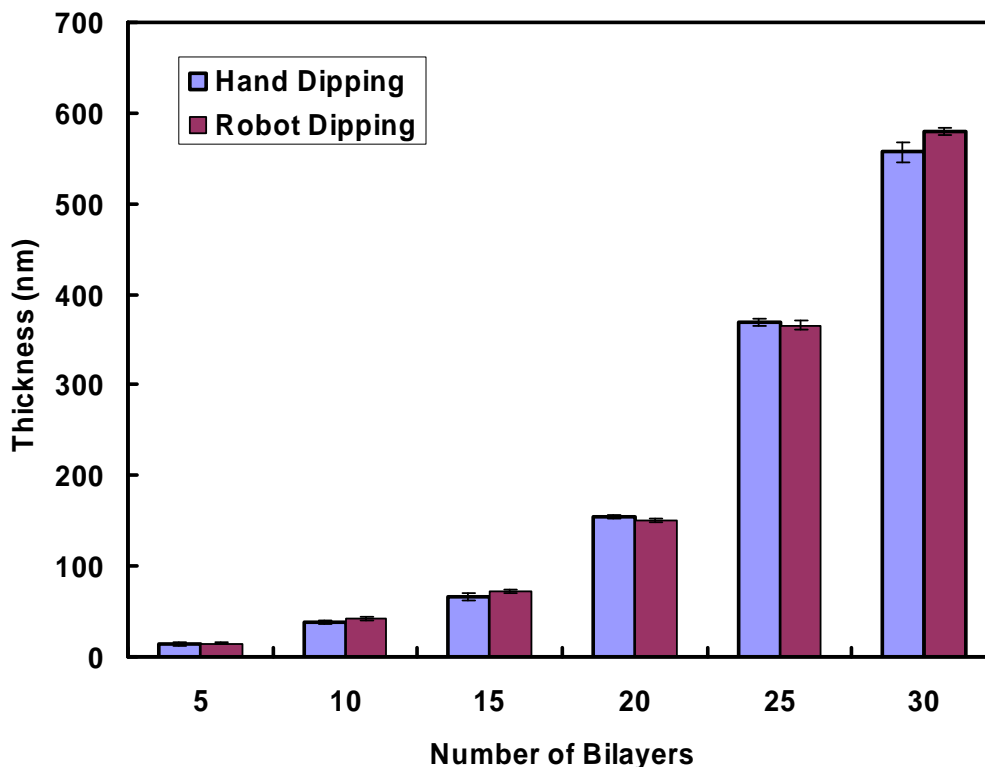


**Figure 23.** Thickness comparison between clay-polyacrylamide assemblies made by hand and with the
robot dipper.

Figure 24 shows a TEM image of a 20-bilayer composite film that was prepared
using the robotic dipping system. The composite substrate is a 175 μm thick
poly(ethylene terephthalate) (PET). This PET film was alternately dipped into aqueous
mixtures containing 1 wt% carbon black (CB) and 0.1 wt% of either polyethylenimine
(PEI) or poly(acrylic acid) (PAA). Prior to dipping, the CB – polymer mixtures were
homogenized with a high speed impeller (operated at 3100 rpm) for 15 minutes and
sonicated for an additional 15 minutes. Sheet resistance of these structures can be tailored
by simply changing the number of bilayers [84], which effectively changes the thickness.

Bulk resistivity ($\rho$) of this 20-bilayer film is obtained by multiplying $R_S$ by thickness ($\sim$ 1.8 μm), which is approximately 0.18 Ω·cm. This value is much lower than most bulk carbon black-filled composites (> 100 μm thick) made with traditional solution [168-169] or melt processing [170-172]. The few bulk composites with comparable resistivity are filled with 40 wt% CB or more [93, 173], making them very brittle and porous. These conductive layers could be alternated with bilayers containing clay [68, 174] to produce thin film, multilayer capacitors using a program like that shown in Figure 22.
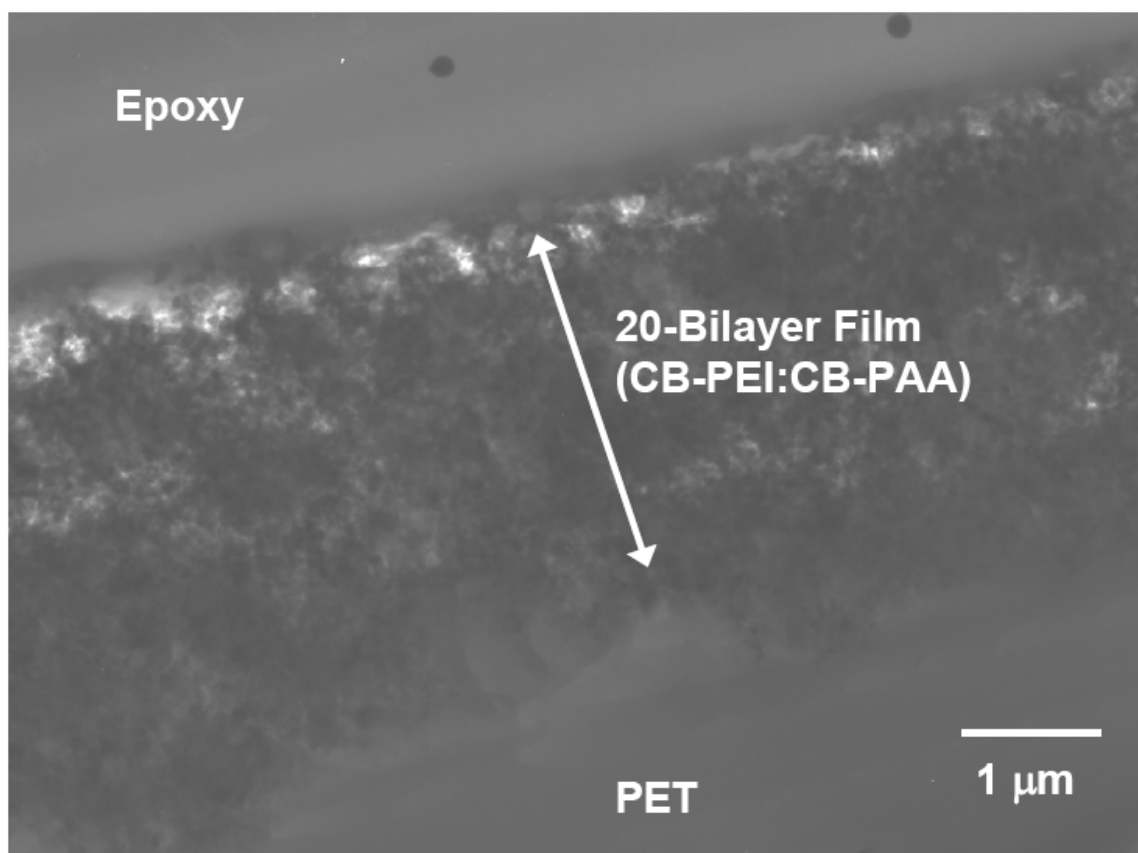


**Figure 24.** TEM image of 20-bilayer film produced by robot using aqueous mixtures of carbon black and charged polymers. The image was obtained with a JEOL JEM 2010 transmission electron microscope operated with an accelerating voltage of 200 kV.

Figure 25 compares the electrical conductivity between hand-dipped films and robot-made carbon black films. The population of hand dipping is three and that of robot

dipping is five for each number of bilayers. The error bars are one standard deviation. ANOVA (see Appendix A) [167] was conducted and no critical difference between hand dipping and robot dipping was found. It should be noted that the number of bilayers was limited to ten, where no siginificant differences would be expected based upon the clay results (see Fig. 23 and discussion on page 46).
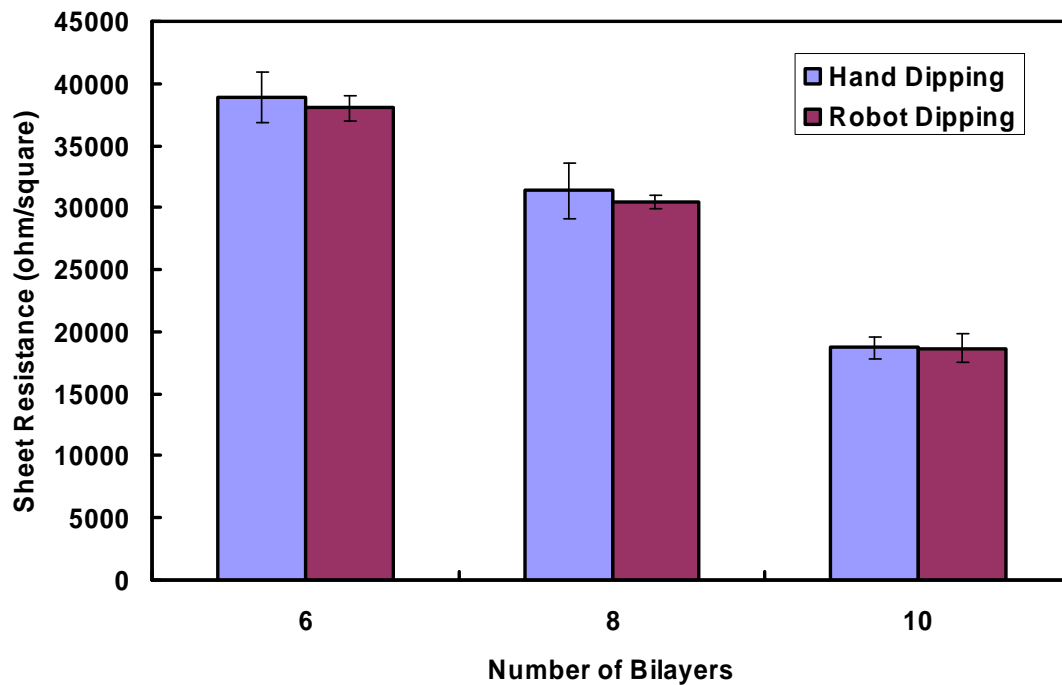


**Figure 25.** Sheet resistance comparison between carbon black assemblies made by hand and with robot dipper.

**3.4 Summary**

Layer-by-layer assembly is a simple, but time consuming process that can be prone to human error. The use of a robotic system demonstrated the ability to build layer-by-layer assemblies without any critical differences from hand dipping up to 25 bilayers. At 30 bilayers a significant discrepancy was found that may be the result of human error.

This thickness difference at 30 bilayers may be the accumulated errors of hand dipping, which can create uneven rinsing and drying (intensity and times). Even if this discrepancy is not of human origin, the robot frees up researcher time for more productive purposes. Additionally, this robot has three-dimensional movements that eliminate the contamination of deposition solutions and films from unexpected mixing of complementary solutions, which is a key advantage relative to other robot dippers. Finally, the programmable procedure allows for a complex dipping order, which provides the ability to make striped structures (e.g., multilayer capacitors) or "quad layers" (i.e., sequential deposition of four ingredients). These more involved recipes would be expected to be more susceptible to human error than the common two ingredient (one cation and one anion) recipes. This robot was used to make all samples for oxygen transmission rate testing described in Chapters IV and V.

**CHAPTER IV**

**OXYGEN BARRIER**

**4.1 Introduction**

Layer-by-layer assembly using polymer and clay is shown to produce thin films with barrier properties that are unrivaled by the technologies described in Chapter II [107].  This unique combination of materials and processing, initially studied at the Avery Research Center [175], can reduce the oxygen transmission rate (OTR) of 179 $\mu$m (7 mil) PET by more than three orders of magnitude without diminishing its transparency or flexibility.  Here it is shown that film thickness increases under two distinct linear regimes as a function of bilayers deposited. The clay concentration in the initial layers is approximately 9 wt.% (4.5 vol.%) during this growth.  A 30-bilayer coating, that is 570nm thick, has an OTR < 0.005cc/m$^2$/day/atm.  This technology suffers from moisture sensitivity, but lamination with a water barrier film allows this low OTR to be maintained at 95%RH.  Unlike other barrier technologies, films made using the LbL process provide both transparency and flexibility, making them a good candidate for foil replacement in a variety of packaging applications.

**4.2 Experimental**

4.2.1 Materials

Cationic polyacrylamide (tradename Superfloc C-491) was provided by CYTEC (West Paterson NJ). This is a copolymer containing 5 mol % of positively-charged repeat units. Southern Clay Products, Inc. (Gonzales, TX) supplied natural, untreated

montmorillonite (MMT) (tradename Cloisite NA$^+$). This clay has a cationic exchange capacity of 0.926 meq/g and is negatively-charged in deionized water. MMT platelets have a density of 2.86 g/cm$^3$, diameter of 10~1000nm, and thickness of 1nm [166]. Polyethylene terephthalate (PET) film, with a thickness of 179μm, was purchased from Tekra (New Berlin, WI) and used as the substrate for LbL deposition. Where inidicated, a polychlorotrifluoroethylene (PCTFE) moisture barrier film (CLARUS$^{TM}$ P4000TR provided by Honeywell) was laminated to the surface of the layer-by-layer coating using Adhesive Transfer Tape 7952MP provided by 3M (St. Paul, MN).

## 4.2.2 Thin Film Preparation

Aqueous solutions of cationic polyacrylamide (0.25wt.% in deionized water) were prepared by rolling for 48 hours. Several concentrations of polyacrylamide solution were examined, but higher concentration had viscosity greater than 1000 cP (i.e., thick syrup) at low shear rates and lower concentration grows much too slowly and unevenly to achieve high barrier. Reproducibility was also an issue at other concentrations because of the issues just described. The viscosity of 0.25wt.% PAm is 500 cP. Suspensions of 0.2wt.% clay in deionized water were similarly prepared. Each 10 x 10cm$^2$ piece of PET film, rinsed with methanol and deionized water, was corona treated with a BD-20C Corona Treater (Electro-Technic Products Inc., Chicago, IL) prior to LbL deposition. The substrate was initially dipped in the PAm solution for five minutes, followed by rinsing with deionized water and blow drying with air. This same procedure was followed with the clay suspension, followed by one minute of deposition for all subsequent dips. Dipping time experiments (10 sec, 30 sec, 1 min, and 5 min) were conducted and film

thickness was found to be independent over this range. One minute was chosen as a compromise because most researchers dip for much greater times. The entire dipping procedure was accomplished with the home-built robotic system described in Chapter III [165].
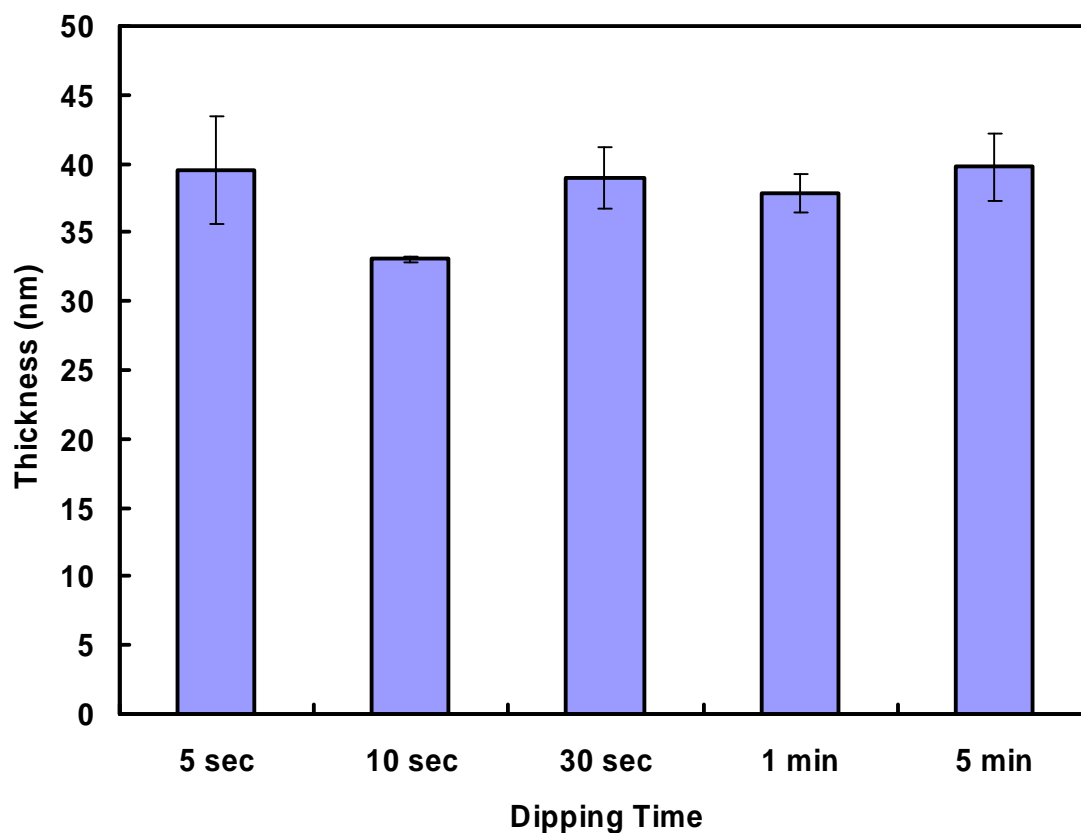


**Figure 26.** Thickness measured via ellipsometry comparing various dip times of 10 bilayer films. Each data point represents three samples and the error bars are one standard deviation.

4.2.3 Film Characterization

Oxygen transmission rate testing was performed by MOCON (Minneapolis, MN) in accordance with ASTM 3985, using an Oxtran 2/21 ML instrument. The test temperature was 23°C and relative humidity was 0% unless otherwise specified. Film

thickness was measured with a PHE-101 Discrete Wavelength Ellipsometer (Microphotonics, Allentown, PA). The laser wavelength is 632.8 nm and a 65° angle of incidence was used. A 1 mm thick, single side polished (100), silicon wafer (University Wafer, South Boston, MA) was used for deposition rather than PET for ellipsometry, so measurements were done only beyond five bilayers to eliminate substrate influence. A quartz crystal microbalance (QCM) (Maxtek Inc., Cypress, CA) was used to measure the mass increase of each deposited layer. A JEOL 1200 EX TEM (Mitaka, Tokyo, Japan) was used to image a cross-section of the LbL film. A Nanoscope IIIA (Veeco Instruments, Woodbury, NY) atomic force microscope (AFM) was used to image the surface of the LbL films. AFM images were obtained in tapping mode using a silicon cantilever tip (MikroMasch, Wilsonville, OR) with a radius of curvature of less than 10 nm. A Zeiss 1530 VP FE-SEM (Thornwood, NY) was used to image a cross-section of the LbL film, while a Bruker-AXS D8 Advanced Bragg-Brentano X-ray Powder Diffractometer (Madison, WI) was used to study the micostructure.

## 4.3 Results and Discussion

4.3.1 Film Growth and Characterization

LbL films typically grow in a linear or exponential manner, depending on the chemistry of the deposited material or ionic strength of the deposition mixture [2, 14, 16, 17, 152, 156]. Figure 26(a) shows the growth of MMT clay and cationic polyacrylamide as a function of bilayers deposited. Each data point represents five samples and the error bars are one standard deviation. A regression tests were used to analyze this data, with Table 5 summarizing the test results. These results implicate simultaneous linear and

quadratic growth trends of PAm/MMT. The linear regression of 15 – 40 bilayer is 0.99

which is significant enough to claim that the growth trend is linear.

**Table 5.** Regression test results of PAm/MMT growth trends.

| Region (Bilayers) | Regression | |
| --- | --- | --- |
| | Linear | Quadratic |
| 5 – 15 | 1 | |
| 5 – 30 | 0.8691 | 0.9925 |
| 5 – 40 | 0.9604 | 0.9835 |
| 15 – 40 | 0.9905 | 0.9911 |

Thinner deposition up to 15 bilayers is believed to be due to a combination of

nonuniform surface coverage and possibly influenced by substrate polarity. This

combination of weak negatively-charged clay and weakly-charged polycation is

relatively unique and the mechanism of this growth is not completely clear. It is believed

that the refractive index of the PAm/MMT assemblies is approximately 1.55 due to the

repeatability of the measured data. Compositional information is provided by a quartz

crystal microbalance (QCM) that measures the weight of each deposited layer.  The data

in Figure 27(b) suggest the composite coating contains approximately 9 wt% clay.  With

a clay density of 2.86g/cm$^3$ and a quartz crystal cross-sectional area of 34.19mm$^2$, the

weight of each clay layer deposited amounts to a thickness of 1.3 nm (i.e., about the

thickness of an individual platelet).  This observation lends support to the assertion that

the clay is deposited as individual exfoliated sheets. Higher numbers of bilayers were too

heavy for the QCM to accurately determine composition in the growth regime beyond 15

bilayers.
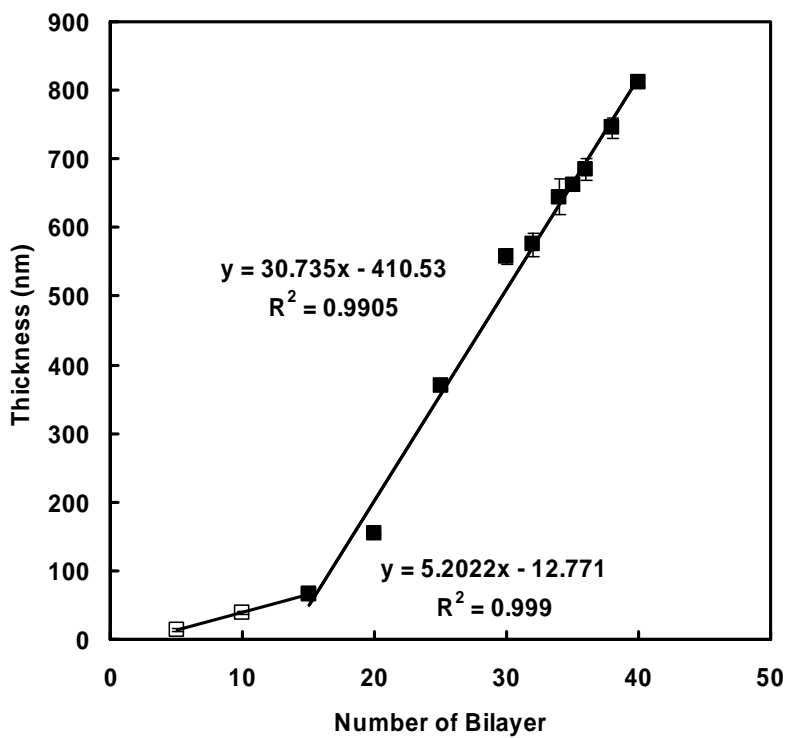
(a)
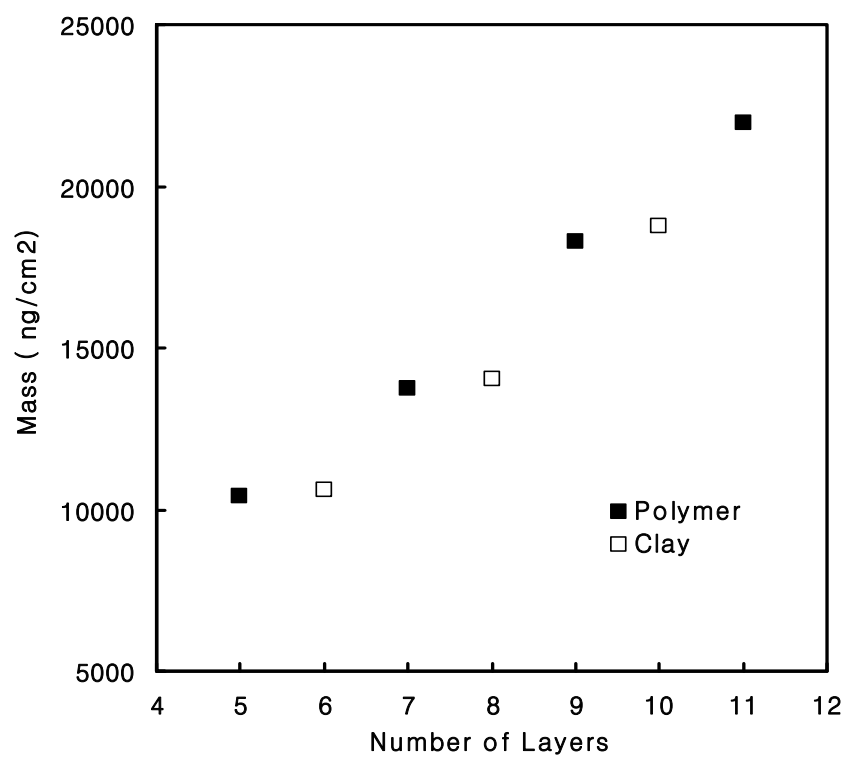


(b)

**Figure 27.** Film thickness as a function of bilayers (a) and weight as a function of the number of individual layers deposited (b) [107].

Evidence of island-like growth was found by depositing one bilayer of MMT clay and cationic polyacrylamide on a formvar TEM grid. The orientation of clay platelets is clearly parallel to the substrate in the TEM image shown in Figure 28. The platelet shape resembles a randomly distributed hexagon, making 2/27 a reasonable estimation of geometric factor for Cussler's permeability model (Eq. 7) [17] discussed in the next section. Figure 28 also illustrates the range of aspect ratios found in natural clay (100 < $\alpha$ < 1000). The average aspect ratio of these clay platelets is ~200, which is similar to that reported in the literature [15]. There are distinct covered and uncovered areas on the TEM grid, which supports the suggestion that uneven coverage of substrate is at least partly responsible for the slope difference seen in the Figure 27(a).
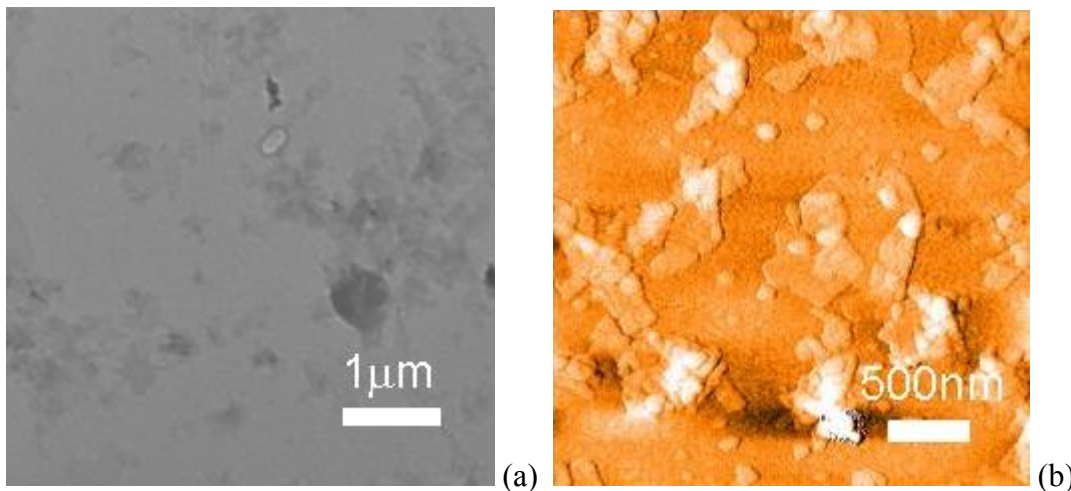


**Figure 28.** TEM surface image of 1.5 bilayer PAm/MMT film (a) and AFM surface image of 1 bilayer of PAm/MMT.

To investigate substrate influence, UV/Vis absorbance was measured as a function of bilayers deposited for assemblies of PAm/MMT on polystyrene. The data shows that the PAm/MMT system is less absorbent on corona treated PS substrate than a non-treated PS substrate. The strong charge density of corona the treated substrate likely

causes the thinner deposition (i.e., lower absorbance). This experiment demonstrates that substrate charge density can significantly alter layer-by-layer growth. Similar experiments done on PET showed strange, but reproducible, absorbance trends that may have something to do with PET's semicrystalline nature and/or self-fluorescence. Figure 29 shows the UV/Vis absorbance data of PAm/MMT as a function of number of bilayers.
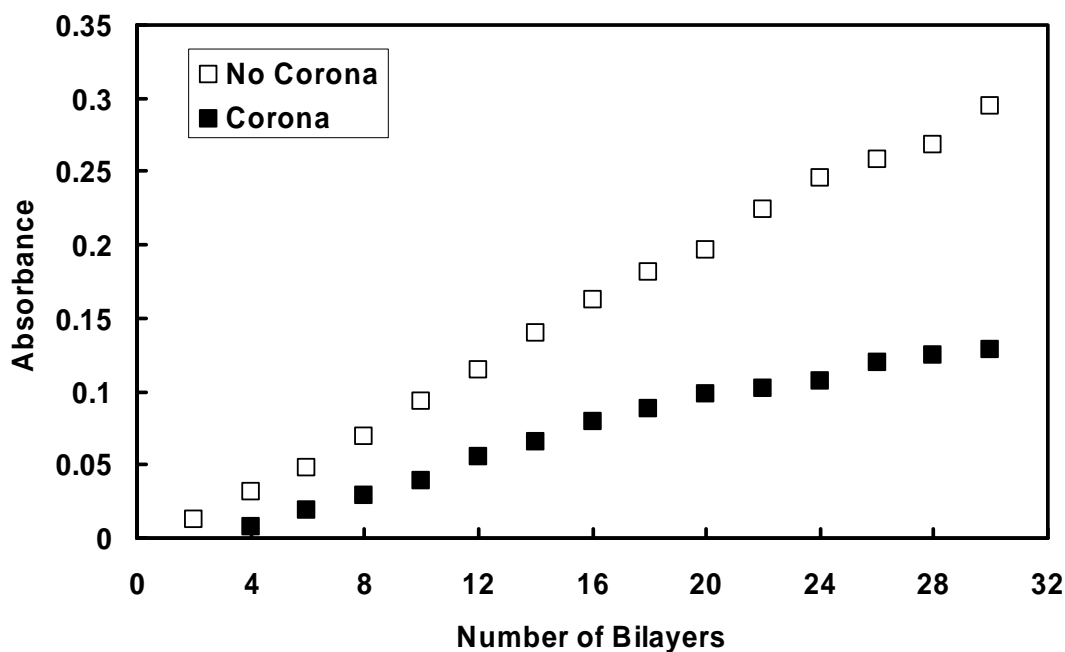


**Figure 29.** UV/Vis absorbance data of PAm/MMT systems on corona treated and non-treated PS.

Figure 30 shows TEM and SEM cross-section images of a 30-bilayer film along with a schematic of the brick wall nanostructure believed to be present. This image shows no evidence of clay aggregates (or intercalated stacks). Figure 31 shows surface images of this film obtained using an atomic force microscope. The height image (Fig. 31(a)) highlights the small surface roughness (approximately 23 nm) that suggests most of the high aspect ratio clay platelets are lying with their largest dimension parallel to the

substrate surface. The surface roughness that does exist may be due to a few platelets overlapping one another and/or loopier deposition of the polyelectrolyte in layers that are further from the substrate [16]. In the phase image (Fig. 31(b)), the clay platelets are more apparent, resembling something like a cobblestone path.



(a)                                        (b)
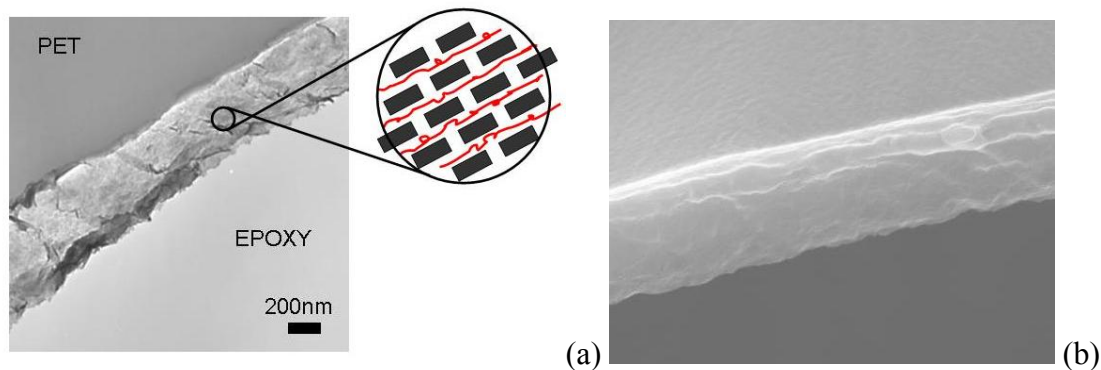
**Figure 30.** TEM [107] (a) and SEM (b) cross-section of a 30-bilayer coating on a PET substrate. This film is believed to have a nanoscale brick wall nanostructure with individual clay platelet bricks and polyacrylamide mortar.



(a)                                        (b)
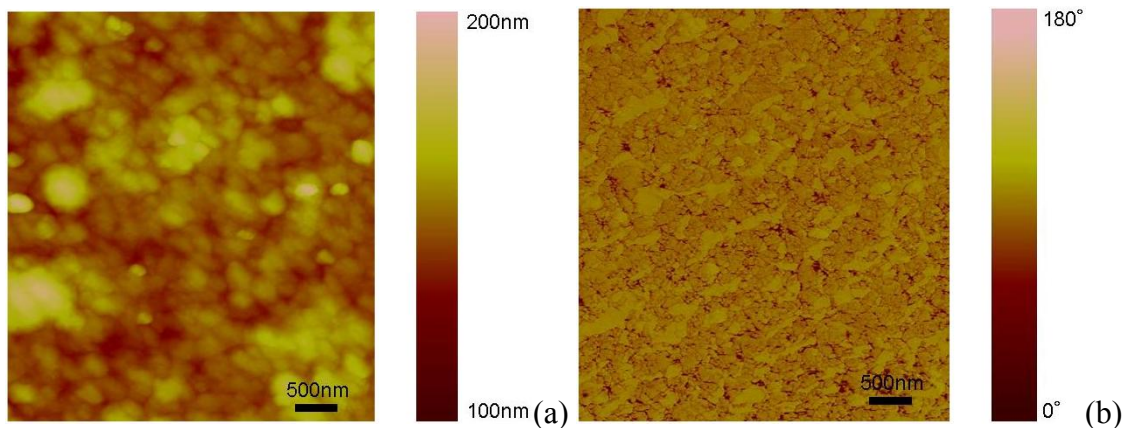
**Figure 31.** AFM height (a) and phase (b) images of the surface of 30-bilayers of cationic polyacrylamide and clay. This film has an RMS surface roughness of 23 nm [107].

X-ray diffraction also suggests that the clay is completely exfoliated in these thin films. Figure 32 shows XRD spectra of 10, 20, and 30-bilayer films. Natural sodium montmorillonite clay typically exhibits a 2θ peak near 7.7 due to the gallery spacing between the stacked plates [176]. In the layer-by-layer assemblies this peak is completely eliminated as the platelets are separated during deposition. The increasing diffuse peak

below a 2θ of 3 is due to the greater spacing created by polymer between the platelets, which is clearly missing perfect order. Others have shown that the clay-filled assemblies are not perfectly spaced multilayers, but rather a more "random tiling of platelets" [177]. The fact that the 2θ peak remains in the same location for all bilayers lends support to the assertion that the films are compositionally similar during growth. Perhaps the strongest evidence for the highly exfoliated brick wall structure, proposed in Fig. 30(a), is the low oxygen transmission rate exhibited by these coatings.
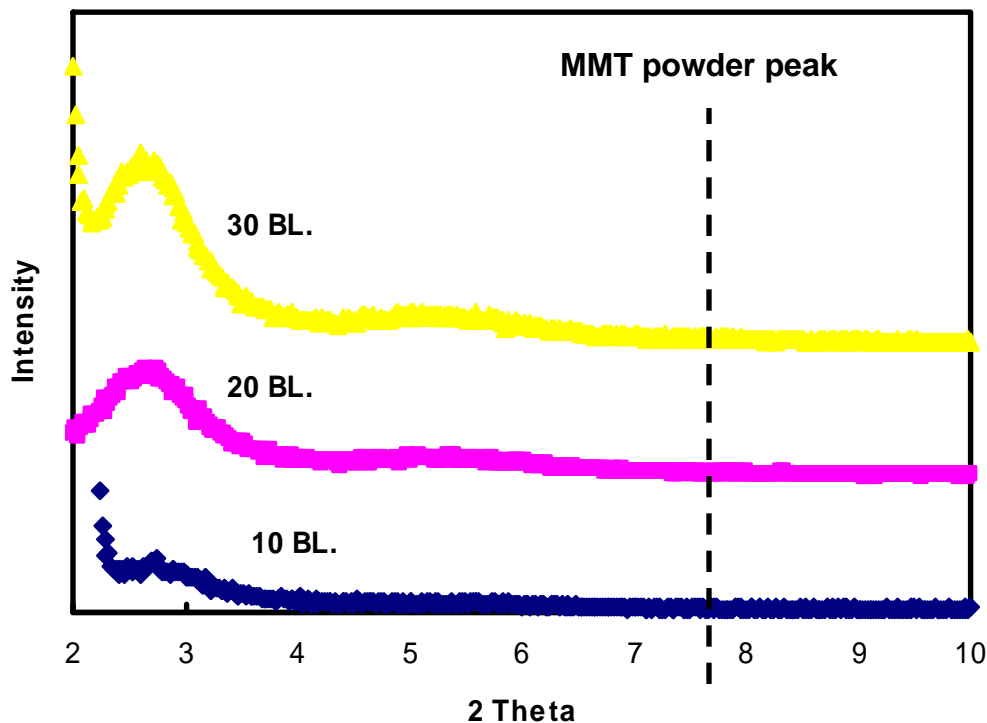


**Figure 32.** Wide angle X-ray diffraction data of 30 bilayer of Pam/MMT films on PET substrate.

4.3.2 Oxygen Permeability

Polyethylene terephthalate has an oxygen permeability of approximately 0.0015cc/m/day/atm [152, 156], making the oxygen transmission rate (OTR) of a 179 $\mu$m film 8.6cc/m$^2$/day/atm. Montmorillonite clay can be thought of as impermeable platelets [17] that reduce the permeability of the polymer matrices it resides in.  Highly exfoliated MMT platelets make the diffusion length longer by creating a tortuous path that reduces the OTR [14-15, 115, 178].  Figure 33(a) highlights the tortuous path concept that was initially proposed by Nielsen [15].  This model assumes a very low concentration of impermeable platelets in a permeable matrix. The platelet aspect ratio is ~200 for MMT [15]. Equation 6 is a good approximation in the dilute regime ($\phi$<<1 and $\alpha\phi$<1) and is typically in reasonable agreement with traditional clay filled polymers [14, 127, 138-139].
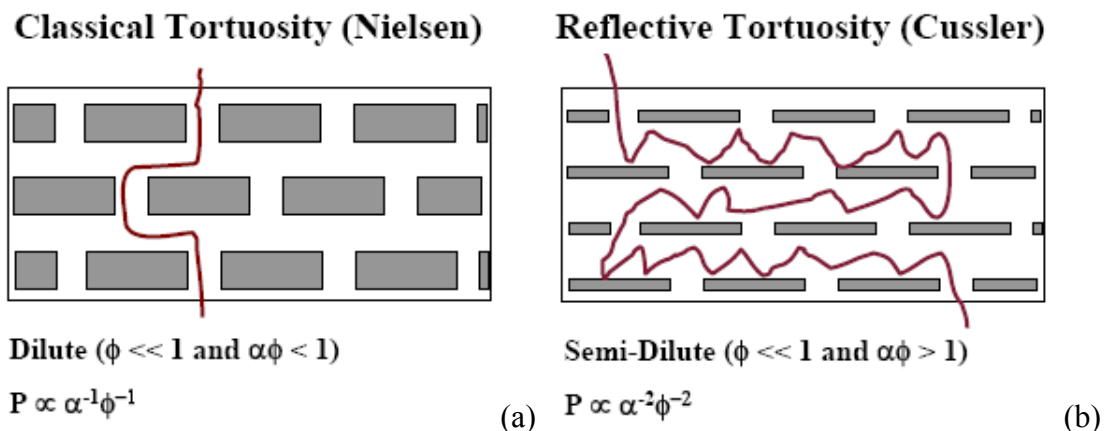


**Figure 33.** Schematic of the classical tortuosity model proposed by Nielsen (a) and the reflective tortuosity proposed by Cussler (b) [107].

More recently, Cussler proposed a model for a composite system in the semi-dilute regime ($\phi$<<1 and $\alpha\phi$>1) that would exhibit a much greater reduction in permeability as a function of platelet concentration [17], as described in Section 2.2.1. In this case, the source of enhanced barrier behavior is an increased length of diffusion

through the composite and decreased cross-sectional area through which the diffusing species can move [119]. This semi-dilute condition is only possible with large platelet aspect ratio (>100) and/or large platelet concentration (> 3 vol%). In traditional clay-filled composites, concentrations greater than 1-2 vol% result in significant clay aggregation that dramatically reduces the effective aspect ratio. Additionally, Equation 7 assumes that all platelets are oriented with their largest dimension perpendicular to the direction of diffusion that requires a "brick wall" nanostructure. Fulfilling all of these criteria is very challenging using traditional solution or melt-processing, but layer-by-layer assembly is able to achieve this specific nanostructure relatively easily.

Figure 34 shows how oxygen transmission rate and permeability decrease with the number of clay-polymer bilayers deposited on PET. Table 6 shows this data, along with film thickness, as a function of bilayers deposited. The permeability of a 20-bilayer coating is similar to SiOx-coated PET [166]. If the permeability of the cationic polyacrylamide is assumed to be $2.83 \times 10^{-6}$ cc/m/day/atm (i.e., the value for a 5-bilayer coating), there is a 500X reduction compared to the 30-bilayer permeability. Table 7 shows back-calculated volume fractions of PAm/MMT assemblies using Cussler's model for the semi-dilute regime (Eq. 7) and Fredrickson's model for the semi-dilute regime (Eq. 12). The aspect ratio of MMT lies between 200 and 800 based on Figure 28. Measured OTR values and an approximated aspect ratio, based on a 1nm platelet thickness, were used to calculate the volume fraction of MMT. Both models suggest a high volume fraction for 30-bilayer films (9.7 vol. % is the lowest using Cussler's semi-dilute model with an aspect ratio of 800). It is clear that a higher aspect ratio generates volume fractions more in line with our experimental observations (~4.5 vol. % below 10 bilayers).

It is difficult to get an accurate clay concentration experimentally for thicker films (> 10 bilayers) due to problems of exceeding QCM sensitivity and inability to produce enough free standing material for TGA. It is possible that the concentration increases at higher bilayers, but it is more likely that these unique films have barrier mechanisms not accounted for by these geometrical models. For example, water-soluble polymers are known to exhibit strong hydrogen bonding that would further slow the rate of oxygen diffusion [179-181].
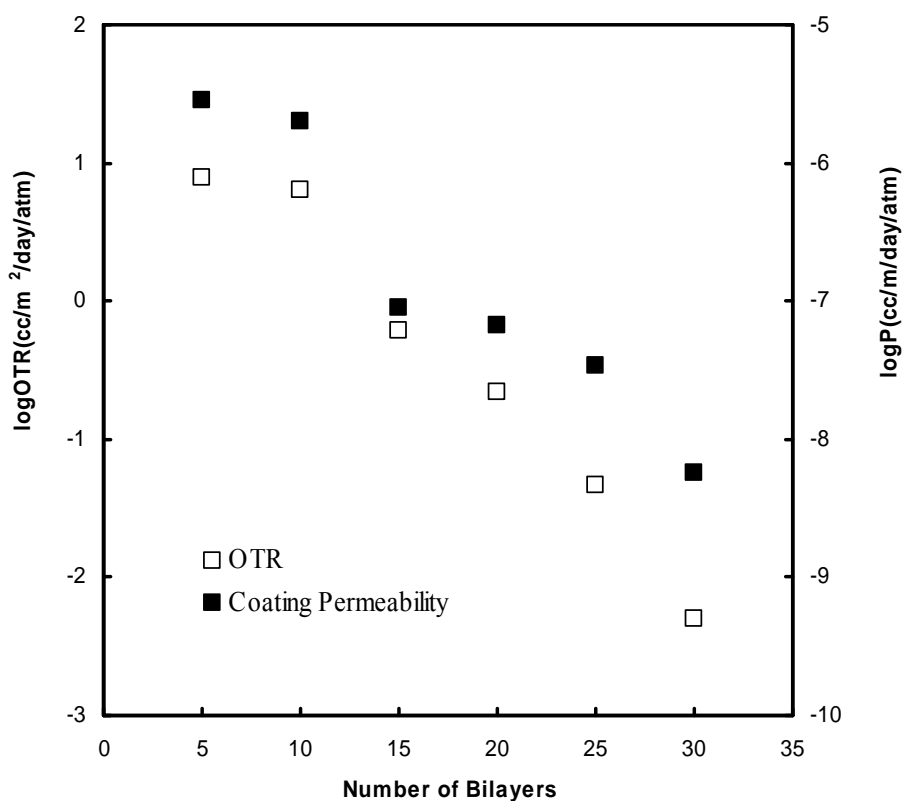


**Figure 34.** Oxygen transmission rate and permeability as a function of the number of bilayers deposited [107]. The OTR values are those of layer-by-layer thin film on a 179 µm PET substrate, while the permeability values are those of the thin film alone decoupled from the substrate (see Table 6).

**Table 6.** Oxygen transmission data for layer-by-layer assemblies [107].

| Number of Bilayers | OTR (cc/m$^2$/day/atm) | Coating Thickness (nm) Coating | Permeability (10$^{-6}$ cc/m/day/atm) Coating[a] | Total |
|---|---|---|---|---|
| 0 | 8.559 | 0 | N/A | 1532.061 |
| 5 | 7.874 | 14.42 | 2.8379 | 1409.673 |
| 10 | 6.417 | 39.13 | 2.0076 | 1149.145 |
| 15 | 0.6045 | 69.18 | 0.0900 | 108.2891 |
| 20 | 0.217 | 148.17 | 0.0660 | 38.9073 |
| 25 | 0.0465 | 366.15 | 0.0342 | 8.3576 |
| 30 | <<0.005 | 571.12 | <<0.0057 | <<0.9007 |

[a] Coating permeability was decoupled from the total permeability using a previously described method [156].

**Table 7.** Volume fraction values PAm/MMT assemblies.

| Number of Bilayers | Volume Fraction (%) Cussler's Model Dilute $\alpha$=200 | $\alpha$=800 | Semi-Dilute[a] $\alpha$=200 | $\alpha$=800 | Fredrickson's Model Dilute[b] $\alpha$=200 | $\alpha$=800 | Semi-Dilute[c] $\alpha$=200 | $\alpha$=800 |
|---|---|---|---|---|---|---|---|---|
| 10 | 0.2 | 0.05 | 1.2 | 0.3 | 0.3 | 0.1 | 2.1 | 0.7 |
| 15 | 15.3 | 3.8 | 9.6 | 2.5 | 25.7 | 8.1 | 17.0 | 5.7 |
| 20 | 21.0 | 5.2 | 11.2 | 2.9 | 35.4 | 11.2 | 19.6 | 6.7 |
| 25 | 41.0 | 10.2 | 15.3 | 4.1 | 69.1 | 21.8 | 26.2 | 9.2 |
| 30 | N/A | 62.1 | 33.4 | 9.7 | N/A | N/A | 52.1 | 21.1 |

[a] Geometric factor is 2/27 for semi-dilute regime of randomly distributed hexagonal impermeable flakes [17].
[b] Geometric factor is $\pi/\ln\alpha$ for dilute regime of randomly distributed disk-type impermeable flakes [21].
[c] Geometric Factor is $\pi^2/(16\ln^2\alpha)$ for semi-dilute regime of randomly distributed disk-type impermeable flakes [21].

4.3.3 Moisture Sensitivity

The best oxygen barrier materials are typically moisture sensitive due to their polar, hydrophilic nature [182]. Montmorrilonite clay completely exfoliates in deionized water and cationic polyacrylamide readily dissolves for this reason. Figure 35 shows the oxygen transmission rate of a 30-bilayer film on PET increase by two orders of magnitude when the humidity is increased from 0% to 65%. Layer-by-layer assemblies are known to swell when exposed to high humidity [183], which effectively decreases the volume concentration of clay platelets and increases the separation distance between them. Despite this increasing permeability, the OTR at 95%RH remains more than an

order of magnitude lower than bare PET. Even with significant swelling the layers

within these thin films are held together with strong electrostatic bonds that prevent

complete loss of barrier behavior. When this system is combined with a high moisture

barrier, an OTR below 0.005 cc/m$^2$/day/atm can be maintained up to 95%RH. Figure 34

demonstrates this effect using a polychlorotrifluoroethylene film laminated to the surface

of the LbL-coated PET. This 101 μm PCTFE film has a moisture vapor transmission rate

of 0.062 g/m$^2$/day/atm and oxygen permeability greater than 0.16 cc/m$^2$/day/atm [1],

making its contribution to the overall laminate oxygen permeability negligible.
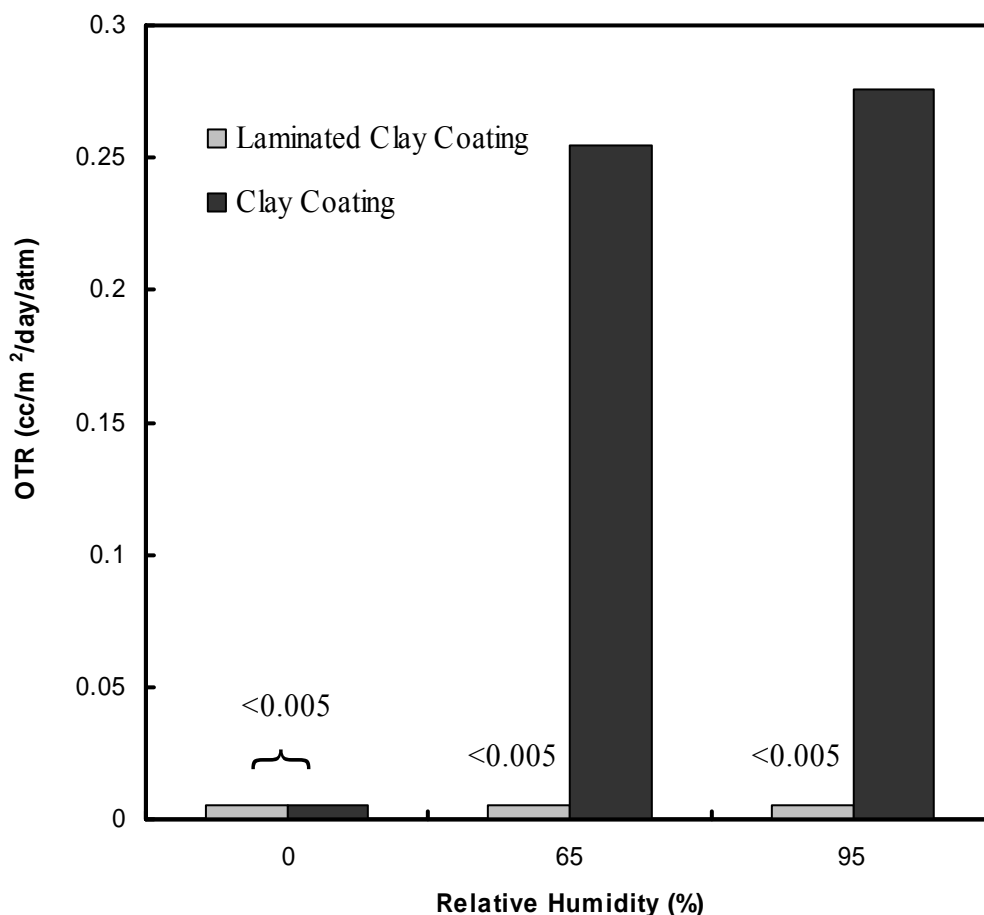


**Figure 35.** Influence of humidity on oxygen transmission rate of 30-bilayer film with and without a PCTFE water barrier laminated to its surface [107].

**4.4 Summary**

Chapter IV focused on LbL coating of PET for reduction of oxygen transmission rate. Thin films, made of negatively-charged montmorillonite clay and a cationic polyacrylamide, were grown on a PET substrate using layer-by-layer deposition. Film thickness increases and oxygen permeability decreases as a function of bilayers deposited. Film growth was measured via ellipsometry and the data were analyzed using the ANOVA test and regression. The results of statistical analysis suggest linear film growth after the initial 10 bilayers. AFM imaging along with a TEM surface image, suggest uneven (island-like) growth of the initial bilayers, resulting in a reduced growth rate. Oxygen permeability below $5.7 \times 10^{-9}$ cc/m/day/atm is achieved after 30-bilayers of clay and polymer deposition, which is an unprecedented value for a polymer composite that is less than 600 nm thick. This high barrier behavior is believed to be due to a brick wall nanostructure present within the thin film that produces an extensive tortuous path for a diffusing oxygen molecule. Experimental data were compared to geometrical models for barrier membranes. Impermeable flakes with a distribution of sizes increases the barrier properties. If flakes are of uniform size only diffusion length is increased, while polydispersed flakes increase the diffusion length and decrease the diffusion volume. Empirical modeling of polydispersed, impermeable flakes would be of value in future work.

The combination of oxygen barrier and transparent properties exhibited by this composite material makes it an ideal candidate for food and electronics packaging. Moisture sensitivity of these films was diminished by laminating a film with high moisture barrier to the surface. Crosslinking of the polyacrylamide is another potential

method for reducing moisture sensitivity that could be studied in the future. Studies of other beneficial properties of these clay-filled thin films are also planned. For example, these films may reduce substrate flammability or impart scratch resistance due to the relatively high concentration (~9 wt.%) of oriented clay. Finally, studies are underway to examine the tailorability of barrier behavior by modifying deposition conditions (e.g., ionic strength of polymer solution), platelet aspect ratio, and polyelectrolyte chemistry. These studies will help refine the understanding of the clay based LbL system via ellipsometry and QCM. In Chapter V, film properties were successfully tailored through modification of polyethylenimine pH.

# CHAPTER V

# pH CONTROLLED GROWTH AND PERMEABILITY

## 5.1 Introduction

The growth of polymer and clay assemblies can be controlled by altering the pH of the deposition mixture [13, 23]. In this chapter, the role of pH in controlling the deposition layer thickness and properties of multilayer thin films fabricated from bilayers of polyethylenimine (PEI) and sodium montmorillonite (MMT) clay, is evaluated. PEI is a weak polyelectrolyte whose charge density changes with pH [184] and this causes its deposition thickness to change [1]. Growth, structure and oxygen permeability of clay-PEI assemblies were studied as a function of pH in an effort to tailor the properties of these thin films. Higher pH results in lower PEI charge density and thicker deposition due to reduced self-repulsion and strong hydrogen bonding. Thicker deposition resulted in reduced oxygen permeability and modulus, which highlights the tailorability of this system.

## 5.2 Experimental

5.2.1 Materials

Branched polyethylenimine was purchased from Aldrich (Milwaukee, WI). This PEI has a molecular weight of 25,000 g/mol. Southern Clay Products, Inc. (Gonzales, TX) supplied natural sodium MMT clay (tradename Cloisite Na$^+$) that was described in Section 4.2.1. The same substrates discussed in Chapter IV (see Section 4.2.1) were also used here.

5.2.2 Thin Film Preparation

Aqueous solutions of PEI (0.1 wt. % in deionized water) were prepared by rolling for 48 hours. Suspensions of 0.2 wt. % clay in deionized water were similarly prepared. Each 5 x 1 cm piece of silicon wafer was rinsed with deionized water and cleaned in a freshly prepared piranha solution (mixture of $H_2SO_4$ and $H_2O_2$ with 7:3 volume ratio) for 1 h. Next, the substrates were rinsed thoroughly with water and dried. Each 10 x 10 cm piece of PET film, rinsed with methanol and deionized water, was corona treated with a BD-20C Corona Treater (Electro-Technic Products Inc., Chicago, IL) prior to LbL deposition. The substrate was initially dipped in the PEI solution for 5 minutes, followed by rinsing with de-ionized water and blow drying with air. This same procedure was followed with the clay solution, followed by one minute of deposition for all subsequent dips. The entire dipping procedure was accomplished with a home-built robotic system (see Chapter III) [165] or hand dipping.

5.2.3 Film Characterization

These clay-PEI assemblies were characterized using all of the same techniques described in Section 4.2.3, with the exception of mechanical property determination. A Nanoindenter XP (CSM, Needham, MA) was used to measure the modulus of these films. Indentation was performed with a diamond Berkovich tip with a 150 nm radius of curvature. The procedure to obtain elastic modulus from the unloading curve of an indentation was previously explained by Oliver and Pharr [185].

## 5.3 Results and Discussion

5.3.1 Film Growth and Characterization

Lowering the pH of the PEI solution increases its positive charge density and extends its chain due to self repulsion, as shown in Figure 36. Figure 37(a) shows how the combination of MMT clay and cationic polyethylenimine (PEI) transition from thinner deposition to thicker deposition as the pH of the PEI deposition solution is increased. The pH of unaltered PEI solution is ~9.5. Film thickness increases with pH of the PEI solution due to reduced polymer charge that results in stronger intermolecular bonding. At low pH, growth is thinner due to like charges repelling each other and extending the PEI chains. When the pH is increased, decreased charge density allows the chain to coil more. Figure 37(b) shows film growth as a function of pH instead of number of bilayers deposited. These PEI-based films exhibit a single linear growth due to the much lower viscosity of the PEI deposition solution (<10 cP) relative to that of PAm (> 500 cP) used in Chapter IV. Lower viscosity promotes uniform coverage of the substrate earlier in the deposition process. Decreasing pH of the PEI solution simply reduces this linear growth and increases clay concentration (see Table 8).
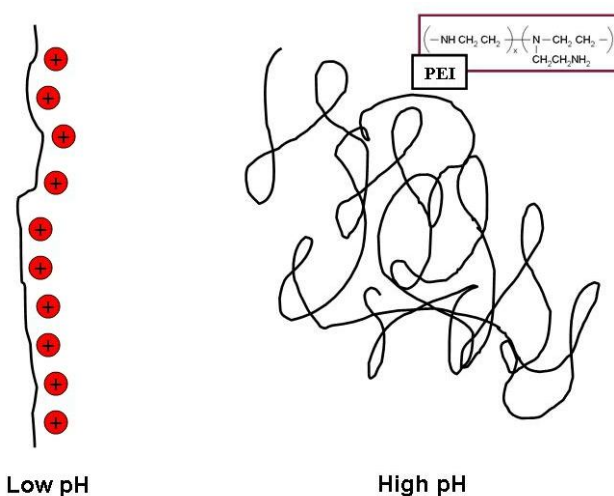


**Figure 36.** Comparison of low charge density and high charge density of PEI.
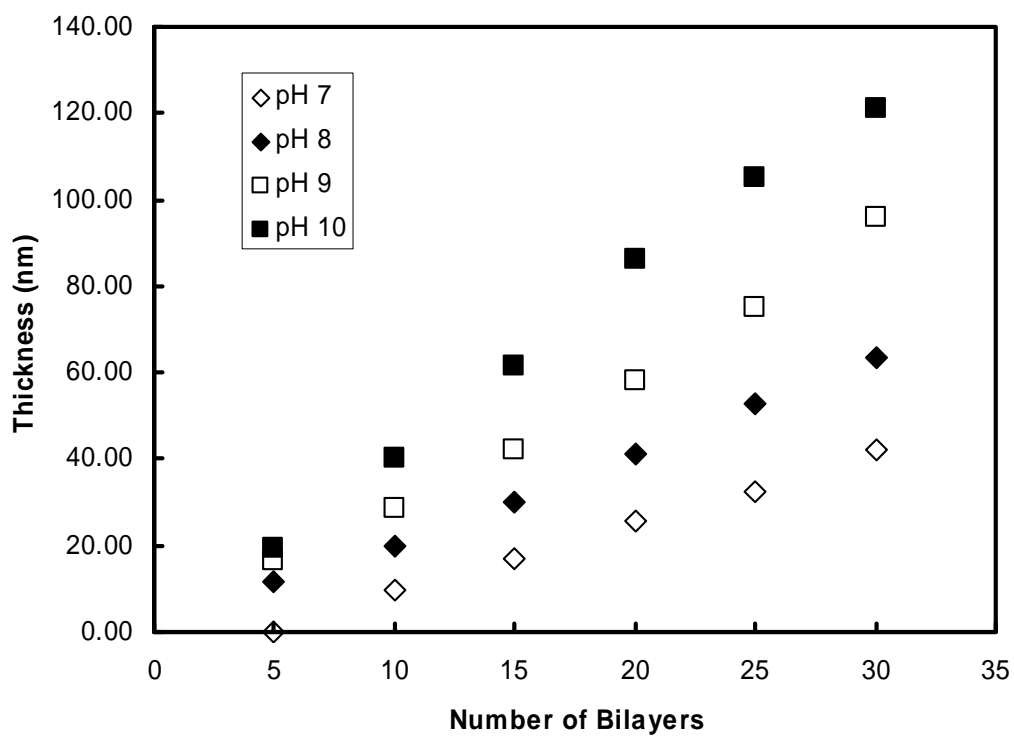
(a)
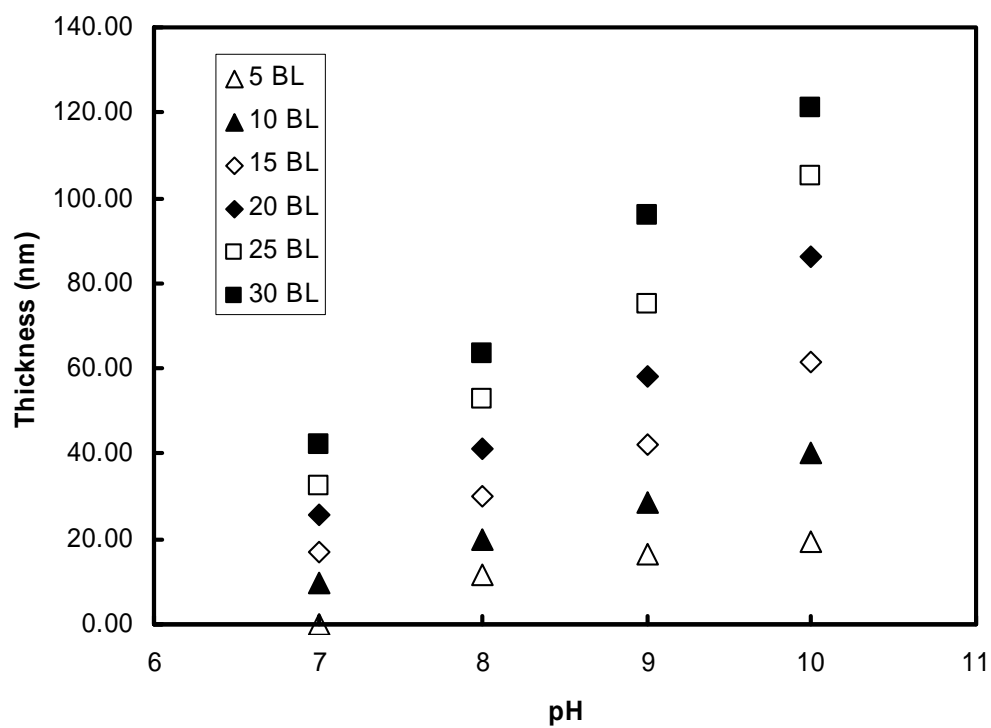


(b)

**Figure 37.** Thickness as a function of the number of bilayers deposited (a) and thickness as a function of pH for various numbers of bilayers (b).

Figure 38 shows an SEM image of the cross-section of a 30-bilayer PEI/MMT film, deposited with PEI having pH=9.5, which is conceptually similar to the PAm/MMT system discussed in Chapter IV. This film is believed to have the same brick wall nano structure, which is depicted in Figure 30(a). The film, deposited on a silicon wafer, was scored and cracked to reveal the cross-section shown here. This image shows no evidence of clay aggregates (or intercalated stacks) and further provides direct confirmation of ellipsometry measurements. Ignoring damage caused during specimen preparation, this film appears to be approximately 160 nm thick, which agrees quite well with the ellipsometry data in Figure 37(a). This cross-section also qualitatively supports the low roughness measured with atomic force microscopy, which will be discussed later.
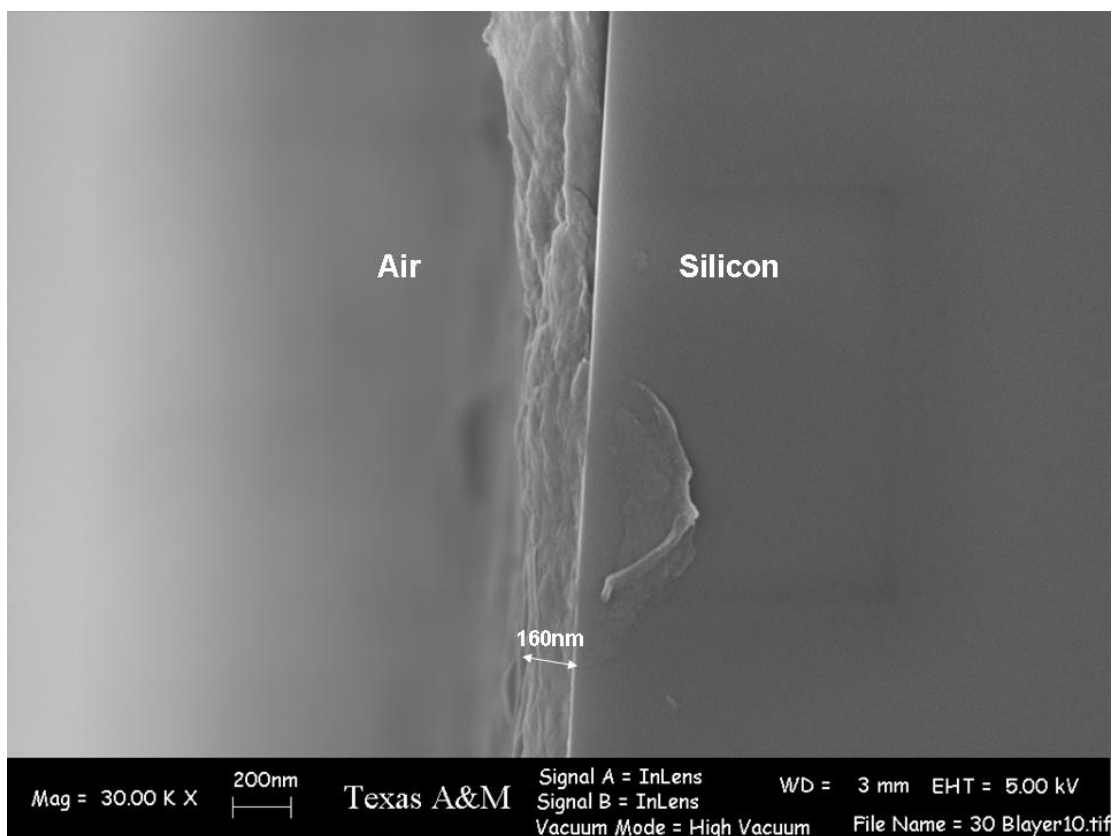


**Figure 38.** SEM image of cross-section of 30 bilayer of PEI/MMT deposited on a silicon wafer.

Atomic force microscope (AFM) height and phase images of PEI/MMT films, shown in Figure 39, reveal the presence of well-aligned clay platelets. The height images show randomly distributed clay platelets uniformly covering the entire surface of the substrate with their faces (i.e., largest dimension) lying parallel to the substrate. Although the phase images have no height information, they do a better job of qualitatively showing the increasing surface roughness with pH. This roughness in the result of thicker, fluffier PEI deposition with increasing pH.
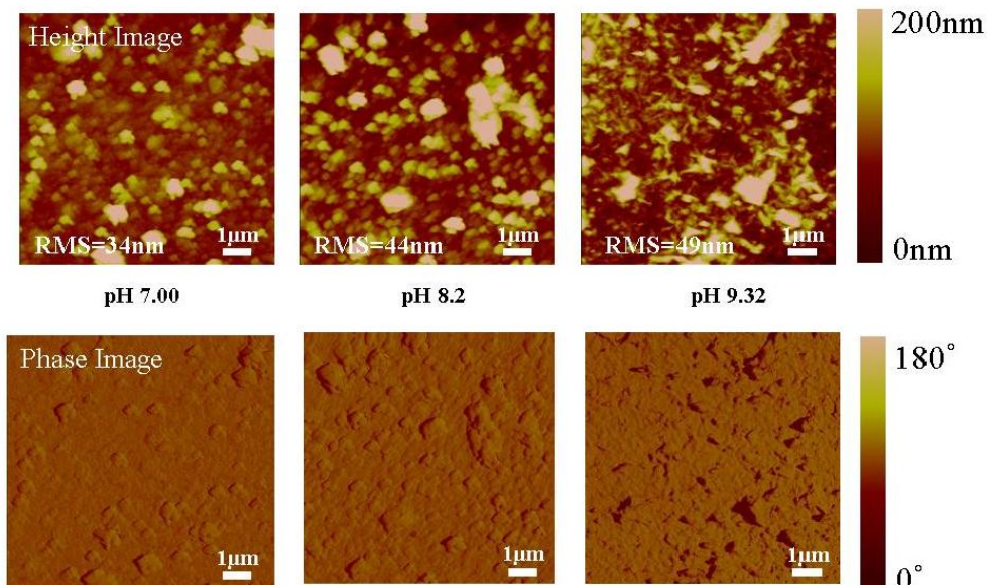


**Figure 39.** AFM height (above) and phase (below) images of the PEI/MMT system at varying pH levels.

Quartz crystal microbalance (QCM) measurements provide compositional information about these films. Figure 40(a) shows that more mass is deposited per bilayer on the gold-coated crystal at higher pH. This result indirectly supports the thickness measurements via ellipsometry (see Fig. 37(a)). If we assume a constant density for all PEI-based films at different pH levels, a greater mass indicates a thicker layer. The density of pure PEI is 1.03 g/cc and that of MMT is 2.86 g/cc. The clay volume fraction, weight fraction, and density of individual bilayers can be calculated assuming this

information is valid. The increasing thickness of PEI layers with pH causes the volume and weight fraction of MMT to decrease. The density of the PEI/MMT films was calculated from the data in Figure 40(a). The density at a pH of 8 is 2.6 g/cc and that at a pH of 10 is 2.1 g/cc. Table 8 summarizes the density and composition of these PEI/MMT films with varying pH. The much thinner deposition of PEI, relative to PAm used in Chapter IV, results in a large increase in MMT concentration.
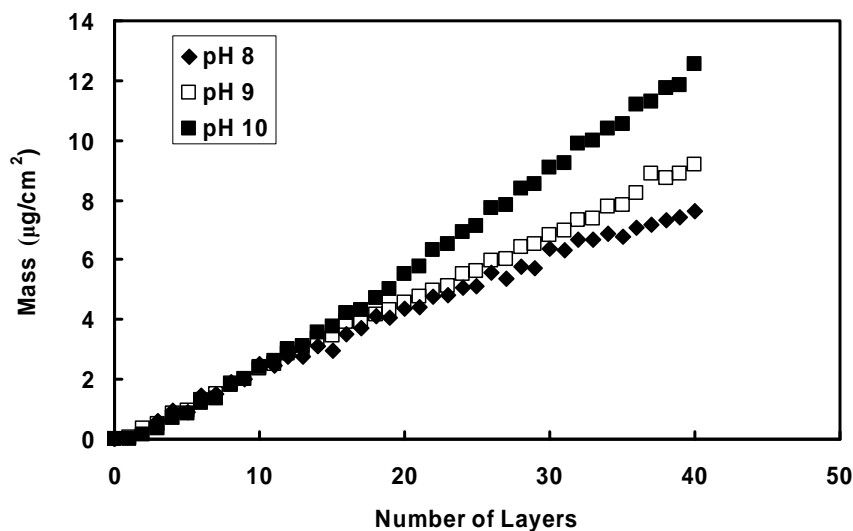
(a)
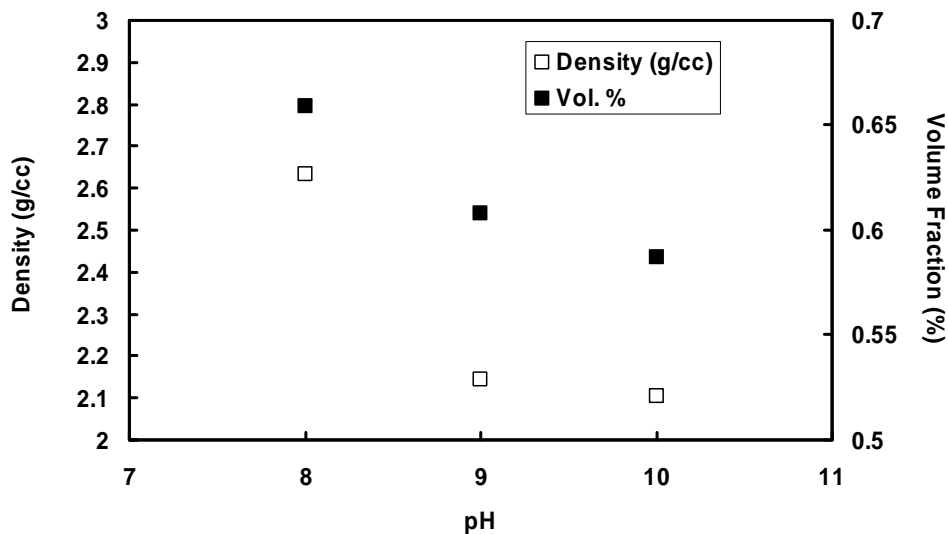
(b)

**Figure 40.** Mass as a function of individual clay and PEI layers deposited (a) and back-calculated density and volume fraction as a function of PEI pH (b). These measurements were made using a quartz crystal microbalance.

**Table 8**. The density and weight percent of PEI/MMT system at varying PEI pH levels.

| pH | MMT (vol. %) | MMT (wt. %) | Density (g/cc) |
|---|---|---|---|
| 8 | 65.8 | 81.6 | 2.63 |
| 9 | 60.8 | 80.0 | 2.14 |
| 10 | 58.7 | 79.2 | 2.10 |

Figure 41 shows the results of wide angle X-ray diffraction (WAXD) performed on neat montmorillonite powder and 30-bilayer assemblies of PEI/MMT at different pH levels. Neat MMT powder exhibits a weak peak at a $2\theta \approx 7.7$. WAXD on PEI/MMT films show decreasing $2\theta$ peak with increasing pH. The d-spacing for these peaks is shown in angstroms in Figure 41. Increasing the spacing between clay platelets from 1.167nm to 1.606nm does not suggest complete exfoliation, but the peaks are relatively diffuse despite the excellent alignment shown in the AFM images (see Fig. 39). There is clearly imperfect vertical spacing between clay layers, as would be expected for the "fuzzy" LbL process [25]. At a pH of 9.54 the peak is especially broad, which suggests that platelet spacing may cover a range that extends more than an order of magnitude. It is also likely that multiple polymer-intercalated platelets occasionally deposit simultaneously, which was discussed in Chapter IV. There is certainly no question that the clay spacing gets broader and larger with increasing pH. This tailorable nanostructure ultimately influences the oxygen permeability and mechanical properties of these films.
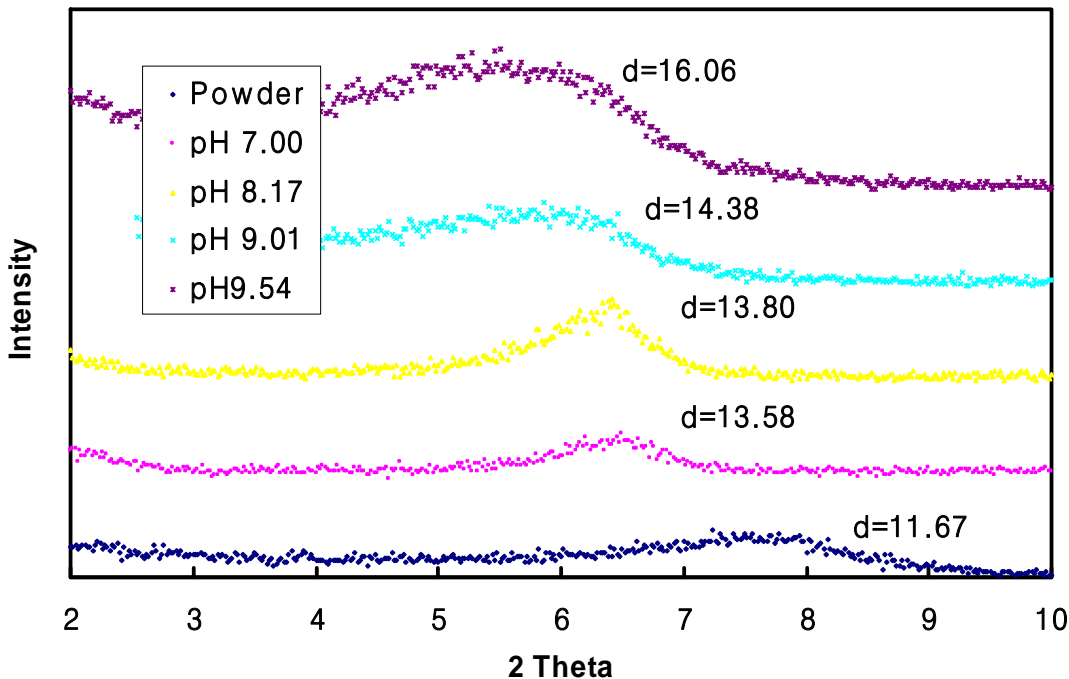
**Figure 41.** Wide angle X-ray diffraction (WAXD) measurements of neat montmorillonite (MMT) powder and PEI/MMT assemblies.

## 5.3.2 Oxygen Permeability

Well exfoliated montmorillonite clay layers can build a tortuous path to block oxygen penetration through a barrier film [17]. However, intercalated clay layers cannot effectively build such a path. Controlling the thickness of PEI between clay layers with pH alteration allows the intercalated layers of clay to become more exfoliated. QCM and X-ray diffraction experiments support this assertion. Table 9 shows the results of permeability measurements performed on 30-bilayer PEI/MMT assemblies at different pH levels of the PEI deposition solution. The permeability of these films is improved by increasing the pH of the PEI solution. The greatest permeability is exhibited at a pH of 7.2. Permeability decreases with increasing PEI pH, which corresponds to greater clay platelet spacing (exfoliation).

**Table 9.** Barrier properties of 30-bilayer assemblies of PEI and clay.

| | OTR (cc/m²·day·atm) | Film Thickness (nm) | Permeability (10⁻⁶ cc/m·day·atm) | |
|---|---|---|---|---|
| | | | Coating[a] | Total |
| PEI pH 7.2 | 5.71 | 45.74 | 0.5223 | 999.77 |
| PEI pH 8.1 | 2.64 | 66.33 | 0.3510 | 462.35 |
| PEI pH 8.7 | 1.63 | 84.50 | 0.2755 | 285.53 |
| PEI pH 9.5 | 0.15 | 108.46 | 0.0325 | 26.28 |

[a] Coating permeability was decoupled from the total permeability using a previously described method [156].

## 5.3.3 Mechanical Properties

Nanocomposites are expected to show improved mechanical properties, but actual values are typically far below the expected theoretical values [186-187]. This discrepancy in mechanical behavior is largely related to the difficulty of achieving good dispersion and exfoliation of nano fillers [58]. As described above, layer-by-layer assembly of clay and PEI can achieve a well dispersed microstructure. Figure 42 shows the results of nanoindentation performed on 30-bilayer assemblies of PEI/MMT at different pH levels. Indentation depth was less than 10 % of total film thickness to avoid any substrate influence. The elastic modulus of pure PEI is essentially zero because it is a viscous liquid at room temperature. A 30-bilayer PEI/MMT film (thickness of 63 nm), made with PEI at pH=8, has an elastic modulus near 20 GPa. This high modulus is due to high concentration and good dispersion of clay in the PEI matrix. It is nearly impossible to achieve this concentration (> 50 vol.%) of well-dispersed clay in a polymer nanocomposite using any other processing techniques. The same 30-bilayer film, made with PEI at pH=9 (thickness is 96 nm), has a modulus of 11.4 GPa. This modulus in lower than pH=8 film due to thicker PEI layers, which reduces clay concentration (see Table 8). Greater modulus (and other property enhancements) could be achieve with crosslinking [62], which is the subject of future work described in Chapter VI. The error

bars in Figure 42 represents one standard deviation, based on more than ten tests at each pH level. The hypothetical mean of the modulus of pure polymer was chosen to be 2 MPa (PEI is actually a thick liquid at room temperature) and a t-test clearly supports the improvement of the modulus of this LbL system.
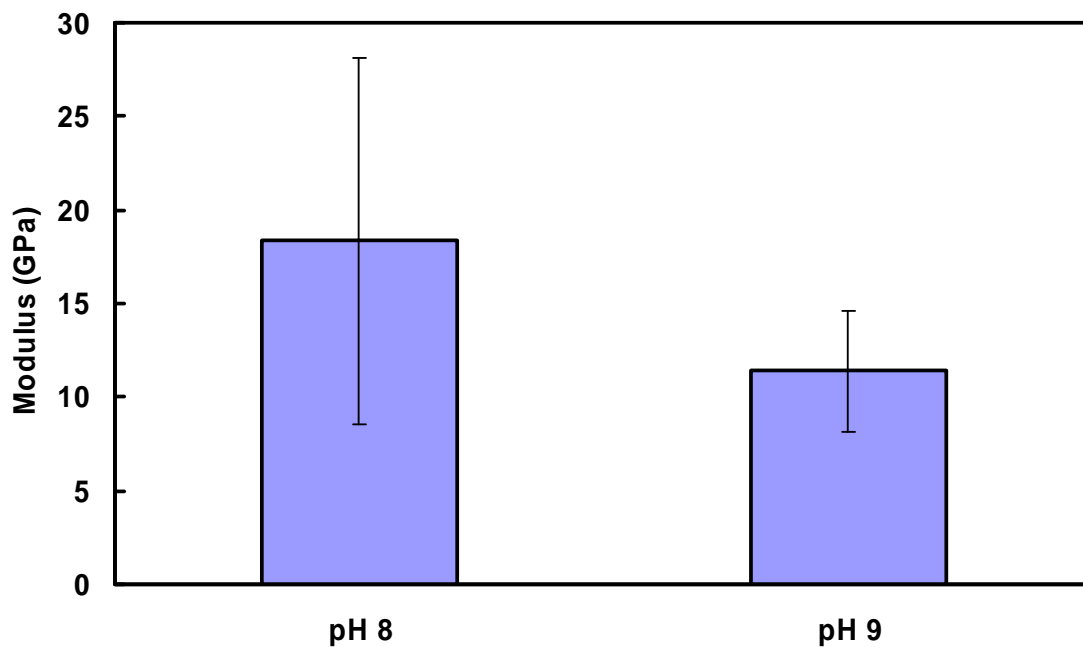
**Figure 42.** Modulus of 30-bilayer PEI/MMT assemblies measured via nanoindentation apparatus.

## 5.4 Summary

Thin films, made of negatively-charged montmorillonite clay and cationic polyethylenimine (PEI), were deposited on PET and silicon wafers using layer-by-layer deposition. Film growth was controlled by altering the pH of polyethylenimine (PEI). This control of film growth was actually polymer layer thickness control that enabled the tailoring of clay exfoliation. Quartz crystal microbalance (QCM), wide angle X-ray

diffraction (WAXD), oxygen transmission rate (OTR), and elastic modulus measurements support this assumption. The QCM measurements allow for a back-calculated thickness of the PEI layer. The thickness of the PEI layer increases with increasing pH of the deposition solution. This increasing thickness of polymer enables the building of a more tortuous path. The WAXD measurements also show an increasing gap between the clay platelets. Oxygen permeability below $91.65\times10^{-9}$ cc/m/day/atm is achieved after 30-bilayers of clay and PEI at a pH of 9.5. This high barrier behavior is believed to be due to a brick wall nanostructure present within the thin film that produces an extensive tortuous path for a diffusing oxygen molecule. Ellipsometry was used to characterize the thickness of the PEI/MMT system. The thickness of a 30-bilayer film built with PEI at a pH of 10 is 121 nm. Scanning electron microscopy was used to confirm the ellipsometery data. The success of this thickness control leads to tailorable barrier and mechanical behavior. In addition to packaging applications, these films have potential for antiflammable coatings and flexible thin film capacitors that will be discussed in Chapter VI.

**CHAPTER VI**

**CONCLUSION AND FUTURE WORK**

The ultimate goal of this thesis work was to prepare and understand the behavior of a transparent, flexible oxygen barrier that is superior to conventional technologies. A series of experiments were performed and analyzed to understand the microstructure and barrier properties of clay and polymer assemblies. Initially, a robotic dipping apparatus was built to provide a means of reproducibly depositing nano-layers of clay and polyelectrolyte from aqueous deposition mixtures (Chapter III). This robot was then used to build high bilayer films with natural montmorillonite clay and a cationic polyacrylamide (Chapter IV) and polyethylenimine (Chapter V), which allowed for tailoring of thickness with pH. Along the way, several directions for future work were discovered and are briefly outlined in Section 6.4.

**6.1 Robotic Dipping System**

Robot-made LbL assemblies have no significant differences from those made by hand dipping. A thickness comparison between robot-dipped and hand-dipped assemblies clearly showed similar film growth and thickness. Time saving is the key advantage of a robotic system, especially when large numbers of bilayers (> 20) are needed. This system, capable of three-dimensional movement, eliminates contamination of deposition solutions and films due to unexpected mixing of complementary solutions. The programmable procedure also allows for a complex dipping order, which provides the ability to make striped structures (e.g., multilayer capacitors). Although not shown here,

it is assumed that reproducibility would be much better with this robotic system. Improvement of rinsing and drying could be achieved using blades instead of nozzles comprised of individual holes.

## 6.2 Oxygen Barrier

Thin films, made of negatively-charged clay and a cationic polyacrylamide, were grown on a PET substrate using layer-by-layer deposition. Film thickness increases and oxygen permeability decreases as a function of bilayers deposited. An undetectable oxygen transmission rate is achieved after 30-bilayers of clay and polymer are deposited. This LbL system can improve food packaging technology and could also be used by the flexible display industry. The flexibility of this PAm/MMT oxygen barrier is unrivaled by current technologies like polymer multilayer [152-155], SiOx [143-151], and bulk composites [157]. The observed high barrier behavior is believed to be due to the brick wall nanostructure present within the thin film that produces an extensive tortuous path for a diffusing oxygen molecule. The alignment and ideal spacing between clay platelets are the critical factors of this work and also the motivation of Chapter V. The current OTR data suggest fully aligned and individual clay platelets, but the influence of clay aspect ratio and crosslinking of the film are yet to be explored. It is possible that an appropriate combination of large and small platelets could reduce the number of bilayers necessary to achieve high barrier behavior. In other words, 20 nm platelets (typical size of synthetic Laponite clay) could potentially fill in gaps between 200-800 nm platelets (typical size range for MMT clay). Crosslinking would densify these films and

potentially reduce moisture sensitivity. This would be especially easy to accomplish with a polymer like polyethylenimine used in Chapter V.

## 6.3 pH Controlled Growth and Permeability

Thin films, made with negatively-charged clay and polyethylenimine, were deposited on PET and silicon wafer (100) using LbL deposition. The spacing between clay platelets was controlled by altering the pH of the PEI deposition solution. This controlling of space between clay platelets means that the nanostructure of these assemblies is highly tailorable. The results of this work indicate that spacing between clay platelets is a major factor controlling the formation of an effective tortuous path, which hinders the diffusion of gas molecules. This research lays the groundwork for thin films with precisely engineered permeability, gas separation, and/or drug delivery. Unlike the PAm used in Chapter IV, PEI has free $-NH_2$ groups that are very reactive with isocyanate species. Figure 43 shows a few examples of multifunctional isocyanates that could effectively crosslink these PEI-based films. Varying the chemistry between the isocyanate groups would allow hydrophobicity to be tailored, perhaps making these films good moisture barriers.
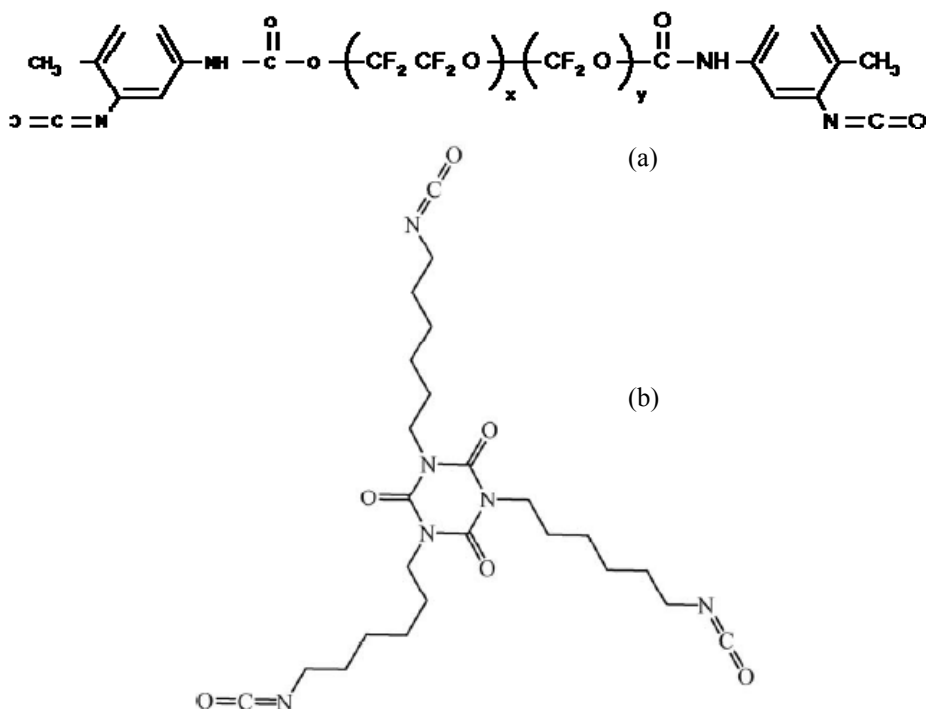
**Figure 43.** Chemical structures of poly(tetrafluoroethylene oxide-co-difluoromethylene oxide) α,ω-diisocyanate (a) and an isocyanurate trimer of hexamethylene diisocyanate (b).

## 6.4 Future Work

There are numerous avenues for additional research in the area of clay-based assemblies with polyelectrolytes. Three of these areas are described in more detail below, including varying the aspect ratio of clay (Section 6.4.1), imparting anti-flammability to foams and fabrics (Section 6.4.2), and studying the dielectric behavior of these films for potential use in thin multilayer capacitors (Section 6.4.3).

### 6.4.1 Clay Aspect Ratio

Oxygen diffusion through a polymer membrane is a relatively mature field of study (more than 30 years of research) [15, 115, 118-122]. Nielson [15] and Cussler [115, 120-122] described the importance of the aspect ratio of impermeable flakes. In the

present work, natural sodium montmorillonite (MMT) was used to improve the barrier properties of PAm/MMT and PEI/MMT assemblies. Clay type is another variable that could be used to alter the barrier properties. Each type of clay has a unique chemistry, crystal structure, and average platelet diameter. There are three forms of layered silicates that each have similar chemistry, crystal structure, and platelet thickness ($\sim$ 1 nm), but differ by orders of magnitude in platelet diameter. Figure 44 shows microscopic images of Laponite, montmorrilonite, and vermiculite clay. Laponite is a synthetic layered silicate (made by Southern Clay Products, Gonzalez, TX) with a platelet diameter of approximately 25 nm [188]. Natural sodium montmorrilonite (Cloisite-Na$^+$ by Southern Clay Products) has an average diameter closer to 150 nm [166]. Vermiculite platelets can be several microns in diameter [189]. Figure 45 highlights the differences in the number of gaps between impermeable platelets with each type of clay deposited within an LbL assembly. With increasing platelet diameter and similar thickness, the gas barrier of composite films made with these clay nanoparticles is expected to increase with increasing aspect ratio [14]. Combinations of these platelets may lead to improved packing that will also enhance barrier.



(a)      (b)      (c)
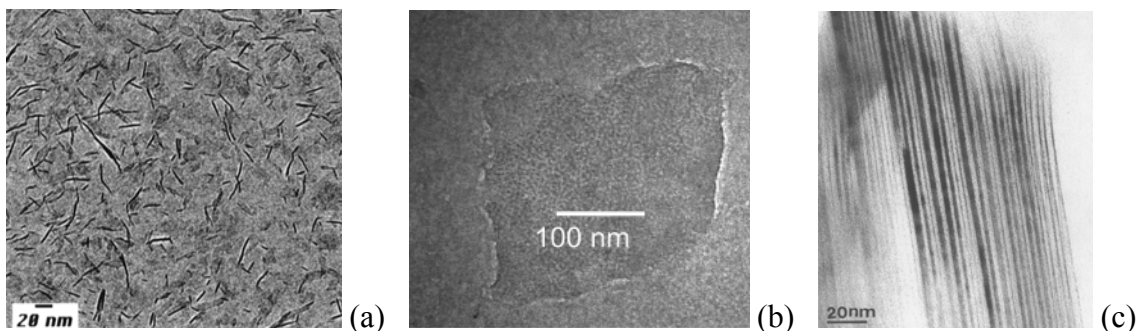
**Figure 44.** TEM images of Laponite in aqueous solution (a) (from Ref. 33), single montmorrilonite platelet (b) (from Ref. 34), and layered stack of vermiculite platelets (c) [188].

**Figure 45.** Schematic images of the nanostructure of clay-based assemblies made with platelets of varying diameters. Each clay-polymer bilayer could be 1 – 30 nm thick depending on deposition conditions.

6.4.2 Anti-Flammable Coating

As of 1998, flame retardants were second only to plasticizers in terms of quantity added to plastics [190]. Brominated compounds are among the most popular retardants, but environmental concerns have led to significant research into the use of more benign nanoparticles such as clays [191-197] and carbon nanotubes [198-200]. These nanocomposites typically exhibit reduced mass loss and heat release rates, which is believed to be due to the formation of a barrier surface layer in the case of clay [192] and a gel-like network in the case of nanotubes [201]. Despite this improved thermal behavior, adding these particles is known to increase processing viscosity and modulus of the final polymeric material [58, 202]. These adverse side effects for flexible foams and fabrics make the need for an alternative technology of vital importance. Layer-by-layer assemblies of polymer and clay can be uniformly applied to the three-dimensional surface of foams and fabrics to impart benefits similar to those seen for bulk nanocomposites.

Proof of concept was established by coating polyurethane foam with 20-bilayers of the clay-polymer oxygen barrier described in Chapter IV. Figure 46 shows what coated and uncoated foam samples looked like following cone calorimeter testing. This test involves exposing the foam to an external heat flux of 11 kW/m from the cone heater and a direct flame for 20 seconds (80 mL/min of propane with 60 mm of water back pressure). The uncoated foam (Fig. 46(a)) exhibited significant flame dripping and was ultimately

destroyed during testing as expected. There was no melt dripping exhibited by the coated sample (Fig. 46(b)). Melt dripping is typically associated with burning foam and is the primary cause of flame spreading. Additionally, the foam coated with 20 BL of PAm/clay showed a dramatically reduced heat release rate (about 50% reduction compared to uncoated foam), as shown in Figure 47. This foam also retained its original shape, as shown in Figure 46(b). These preliminary results suggest that these clay-filled thin films could be an effective flame suppressant. Additional work is needed to evaluate the effect of number of bilayers and film composition, much like for barrier.



(a)　　　　　　　　(b)
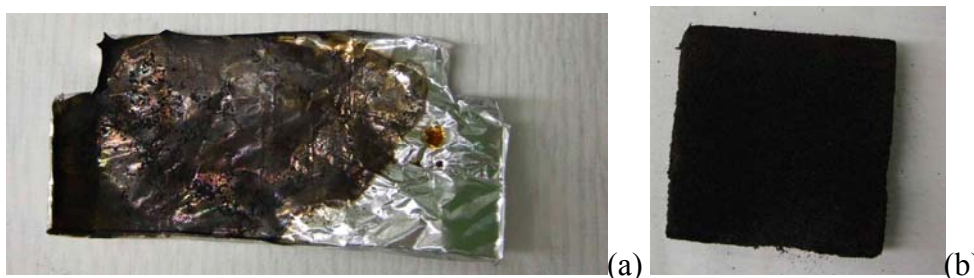
**Figure 46.** Images of uncoated polyurethane foam (a) and foam coated with 20-bilayers of clay and cationic polyacrylamide (b) following cone calorimeter testing performed at NIST (Gaithersbury, MD).
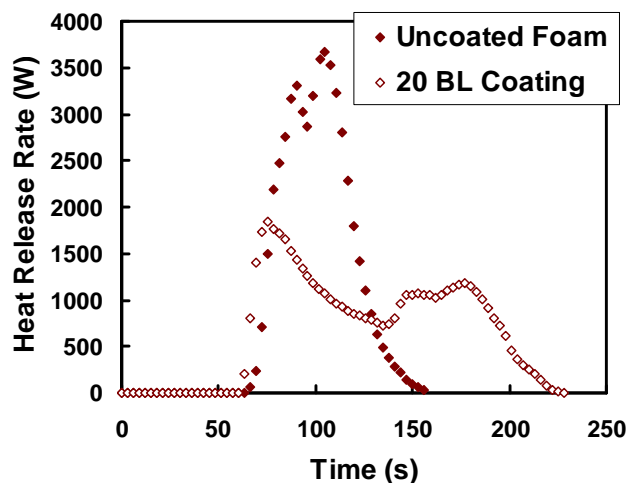


**Figure 47.** Heat release rate as a function of time from vertical cone calorimeter tests of uncoated polyurethane foam (Control) and foam coated with 20-bilayers of clay and cationic polyacrylamide.

6.4.3 High Dielectric Thin Flims

Clay is a relatively high dielectric constant material ($\varepsilon \sim 200$) [203], so LbL assemblies with clay may exhibit higher dielectric than traditional bulk polymer composites. An initial experiment, measuring the capacitance of 30 BL PAm/MMT between gold electrodes, suggested this film had a dielectric constant of 7~8. Higher values may be possible by depositing thinner polymer layers. Deposition of this high dielectric material in between sections of electrically conductive assemblies [204] would result in a thin multilayer capacitor. Figure 48 shows how such a structure could be generated. These thin capacitors, shown in Figure 48, would be useful for pressure sensing and energy storage in applications requiring light weight and flexibility.
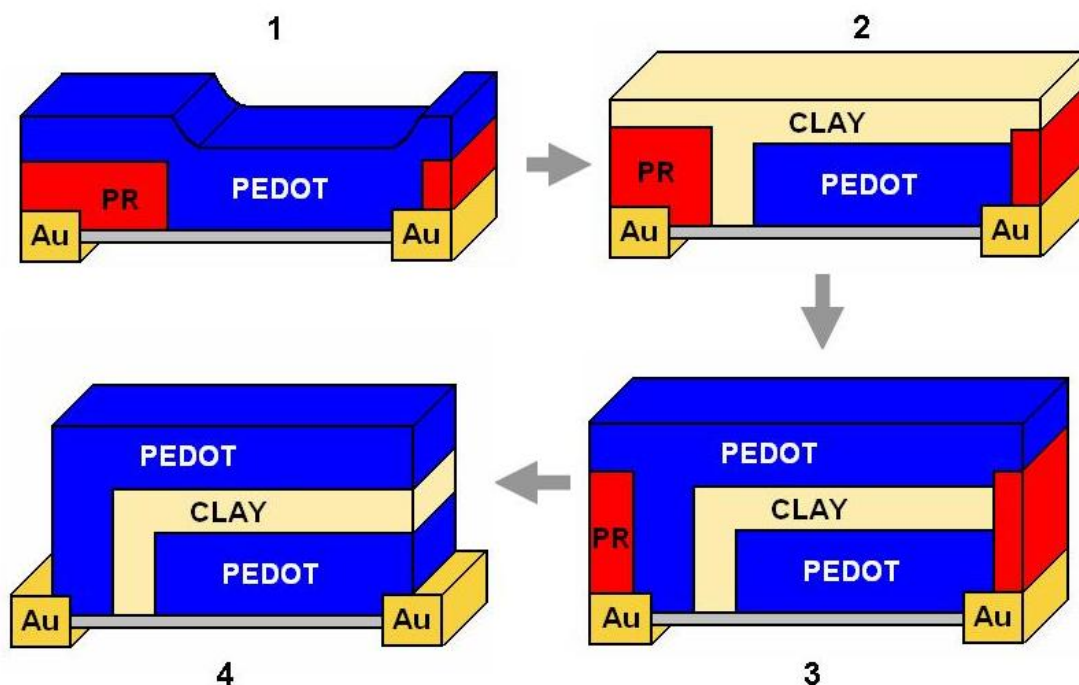


**Figure 48.** Thin, transparent capacitors could be produced using layer-by-layer assembly and traditional photolithography.

# REFERENCES

1. P Bertrand, A Jonas, A Laschewsky, R Legras, Macromol. Rapid Comm. 21 (2000) 319.

2. G Decher, JB Schlenoff, Multilayer thin films: sequential assembly of nanocomposite materials, Wiley-VCH: Weinheim, Germany, 2003.

3. CM Nolan, MJ Serpe, LA Lyon, Biomacromolecules 5 (2004) 1940.

4. JH Kim, SH Kim, S Shiratori, Sens. Actuat. B 102 (2004) 241.

5. DM DeLongchamp, PT Hammond, Langmuir 20 (2004) 5403.

6. GJ Yao, BQ Wang, YP Dong, MF Zhang, ZH Yang, QL Yao, LJW Yip, BZ Tang, J. Polym. Sci. A Polym. Chem. 42 (2004) 3224.

7. R von Klitzing, B Tieke, Adv. Polym. Sci. 165 (2004) 177.

8. O Mermut, CJ Barrett, Journal of Physical Chemistry B 107 (2003) 2525.

9. ZJ Sui, D Salloum, JB Schlenoff, Langmuir 19 (2003) 2491.

10. HL Tan, MJ McMurdo, G Pan, PG Van Patten, Langmuir 19 (2003) 9311.

11. H Zhang, J Ruhe, Macromolecules 36 (2003) 6593.

12. RA McAloney, M Sinyor, V Dudnik, MC Goh, Langmuir 17 (2001) 6655.

13. SS Shiratori, MF Rubner, Macromolecules 33 (2000) 4213.

14. RK Bharadwaj, AR Mehrabi, C Hamilton, C Trujillo, M Murga, R Fan, A Chavira, AK Thompson, Polymer 43 (2002) 3699.

15. LE Nielsen, J. Macromol. Sci. (Chem.) A1(5) (1967) 929.

16. X Arys, AM Jonas, B Laguitton, R Legras, A Laschewsky, E Wischerhoff, Prog. Org. Coat. 34 (1998) 108.

17. JP Derocher, BT Gettelfinger, J Wang, EE Nuxoll, EL Cussler, J. Membr. Sci. 254 (2005) 21.

18. MR Kamal, IA Jinnah, Polym. Eng. Sci. 24 (1984) 1337.

19. Data Sheet, SELAR OH Barrier Resins, EI DuPont De Nemours and Company, Wilmington, DE (1990).

20. WT Brydges, ST Gulati, G Baum, J. Mater. Sci. 10 (1975) 301.

21. GH Fredrickson, J Bicerano, Journal of Chemical Physics 110 (1999) 2181.

22. B Schoeler, E Poptoshev, F Caruso, Macromolecules, 36 (2003) 5258.

23. J Choi, MF Rubner, Macromolecules 38 (2005) 116.

24. J Suh, HJ Paik, BK Hwang, Bioorganic Chemistry 22 (1994) 318.

25. G Decher, Science 277 (1997) 1232.

26. RK Iler, Journal of Colloid and Interface Science 31 (1966) 569.

27. G Decher, JD Hong, J Schmitt, Thin Solid Films 210/211 (1992) 831.

28. JB Schlenoff, Hiep Ly, M Li, J. Am. Chem. Soc. 120 (1998) 7626.

29. Y Lvov, G Decher, M Höhwald, Langmuir 9 (1993) 481.

30. JJ Ramsden, YM Lvov, G Decher, Thin Solid Films 254 (1995) 246.

31. G Decher, J Schmitt, Progress in Colloid & Polymer Science 89 (1992) 160

32. DL Elbert, CB Hebert, JA Hubbell, Langmuir 15 (1999) 5355.

33. C Picart, J Mutterer, L Richert, Y Luo, GD Prestwich, P Schaaf, JC Voegel, P Lavalle, PNAS 99 (2002) 12531.

34. P Lavalle, C Gergely, FJG Cuisinier, G Decher, P Schaaf, JC Voegel, C Picart, Macromolecules 35 (2002) 4458.

35. JH Cheung, AF Fou, MF Rubner, Thin Solid Films 244 (1994) 985.

36. M Ferreira, MF Rubner, Macromolecules 28 (1995) 7107.

37. J Ruths, F Essler, G Decher, H Riegler, Langmuir 16 (2000) 8871.

38. DK Kim, SW Han, CH Kim, JD Hong, K Kim, Thin Solid Films 250 (1999) 153.

39. RA McAloney, V Dudnik, MC Goh, Langmuir 19 (2003) 3947.

40. RA Advincula, E Aust, W Meyer, W Knoll, Langmuir 12 (1996) 3536.

41. V Pardo-Yissar, E Katz, O Lioubashevski, I Willner, Langmuir 17 (2001) 1110.

42. Y Cheng, RM Corn, J. Phys. Chem. B 103 (1999) 8716.

43. C Picart, P Lavalle, P Hubert, FJG Cuisinier, G Decher, P Schaff, JC Voegel, Langmuir 17 (2001) 7414.

44. YM. Lvov, G Decher, Crystallogr. Rep. 39 (1994) 628.

45. G Ladam, P Shaad, JC Voegel, P Schaaf, G Decher, F Cuisinier, Langmuir 16 (2000) 1249.

46. L Kolarik, DN Furlong, H Joy, C Struijk, R Rowe, Langmuir 15 (1999) 8265.

47. K Büscher, G Karlheinz, H Ahrens, CA Helm, Langmuir 18 (2002) 3585.

48. ST Dubas, JB Schlenoff, Macromolecules 32 (1999) 8153

49. H Mattoussi, LH Radzilowski, BO Dabbousi, EL Thomas, MG Bawendi, MF Rubner, J. Appl. Phys. 83 (1998) 7965.

50. FG Aliev, MA Correa-Duarte, A Mamedov, JW Ostrander, M Giersig, LM Liz-Marzan, NA Kotov, Adv. Mater. 11 (1999) 1006.

51. T Vossmeyer, B Guse, I Besnard, RE Bauer, K Mullen, A Yasuda, Adv. Mater. 14 (2002) 238.

52. J Park, LD Fouche, PT Hammond, Adv. Mater. 17 (2005) 2575.

53. MMJ Treacy, TW Ebbesen, JM Gibson, Nature 381 (1996) 678.

54. MF Yu, O Lourie, MJ Dyer, K Moloni, TF Kelly, RS Ruoff, Science 287 (2000) 637.

55. O Breuer, U Sundararaj, Polym. Compos. 25 (2004) 630.

56. GV Lier, CV Alsenoy, VV Doren, P Geerlings, Chem. Phys. Lett. 326 (2000) 181.

57. A Sturcova, GR Davies, SJ Eichhorn, Biomacromolecules 6 ( 2005) 1055.

58. OL Manevitch, GC Rutledge, J. Phys. Chem. B 108 (2004) 1428.

59. JJ Mack, LM Viculis, A Ali, R Luoh, G Yang, HT Hahn, FK Ko, RB Kaner, Adv. Mater. 17 (2005) 77.

60. MASA Samir, F Alloin, A Dufresne, Biomacromolecules 6 (2005) 612.

61. SS Ray, M Okamoto, Prog. Polym. Sci. 28 (2003) 1539.

62. P Podsiadlo, AK Kaushik, EM Arruda, AM Waas, BS Shim, J Xu, H Nandivada, BG pumplin, J Lahann, A Ramamoorthy, NA Kotov, Science 318 (2007) 80.

63. FG Aliev, MA Correa-Duarte, A Mamedov, JW Ostrander, M Giersig, LM Lis-Marzán, NA Kotov, Advanced Materials 11 (1999) 1006.

64. Z Tang, NA Kotov, S Magonov, B Ozturk, Nature Materials 2 (2003) 413.

65. P Podsiadlo, Z Tang, BS Shim, NA Kotov, Nano Letters 7 (2007) 1224.

66. D Ingersoll, PJ Kulesza, LR Faulkner, J. Electrochem. Soc. 141 (1994) 140.

67. NA Kotov, I Dekany, JH Fendler, J. Phys. Chem. 99 (1995) 13065.

68. AA Mamedov, NA Kotov, M Prato, DM Guldi, JP Wicksted, A Hirsch, Nat. Mater. 1 (2002) 190.

69. C Jiang, H Ko, VV Tsukruk, Adv. Mater. 17 (2005) 2127.

70. A Sellinger, PM Weiss, A Nguyen, Y Lu, RA Assink, W Gong, CJ Brinker, Nature 394 (1998) 256.

71. XW Fan, M Park, C Xia, R Advincula, Journal of Materials Research 17 (2002) 1622.

72. AG Evans, Z Suo, RZ Wang, IA Aksay, MY He, JW Hutchinson, Journal of Materials Research 16 (2001) 2475.

73. S Weiner, HD Wagner, Annu. Rev. Mater. Sci. 28 (1998) 271.

74. L Greenemeier, Scientific American, News-October 11 2007 [http://www.sciam.com/article.cfm?id-8F6AA474-E7F2-99DF-3332C34C30DF9269&prin…].

75. R Dagani, Chem. Eng. News 79 (2001) 40.

76. A Seeboth, J Schneider, A Patzak, Sol Energy Mater. Sol. Cells 60 (2000) 263.

77. M Green, Chem. Ind. 17 (1996) 641.

78. PMS Monk, RJ Mortimer, DR Rosseinsky, Electrochromism: Fundamentals and Applications; Weinheim: New York 1995.

79. RJ Mortimer, Electrochimica Acta 44 (1999) 2971.

80. U Bach, D Corr, D Lupo, F Pichot, M Ryan, Advanced Materials 14 (2002)845.

81. DM DeLongchamp, M Kastantin, PT Hammond, Chem. Mater. 15 (2003) 1575.

82. DM DeLongchamp, PT Hammond, Advanced Materials 13 (2001) 1455.

83. P Podsiadlo, ZY Tang, BS Shim, NA Kotov, Nano Letter 7 (2007) 1224.

84. NA Galiote, G Huguenin, Journal of Physical Chemistry C 11 (2007) 14911.

85. WS Alencar, FN Crespilho, MRMC Santos, V Zucolotto, ON Oliveira,WC Silva, Journal of Physical Chemistry C 111 (2007) 12817.

86. JC Grunlan in Organic and Nanocomposite Optical Materials, Mater. Res. Soc. Proc. 846 (2005) 289.

87. CJ Jan, MD Walton, EP Mc Connell, WS Jang, YS Kim, JC Grunlan, Carbon, 44 (2006) 1974.

88. T Dawidczyk, MD Walton, W Jang, JC Grunlan, Langmuir in press.

89. BS Shim, ZY Tang, MP Morabito, A Agarwal, HP Hong, NA Kotov, Chemistry of Materials 19 (2007) 5467.

90. L Supriya, RO Claus, Journal of Physical Chemistry B 109 (2005) 3715.

91. K Cheah, GP Simon, M Forsyth, Polymer Int. 50 (2001) 27.

92. GJ Lee, KD Suh, Polymer Eng. Sci. 38 (1998) 471.

93. JF Feller, I Linossier, G Levesque, Polymers, Adv. Technol. 13 (2002) 714.

94. H Tang, XF Chen, YX Luo, Eur. Polymer J. 32 (1996) 963.

95. R Schueler, J Petermann, K Schulte, HP Wentzel, J. Appl. Polymer Sci. 63 (1997) 1741.

96. JC Grunlan, WW Gerberich, LF Francis, J. Mater. Res 17 (1999) 4132.

97. FG Souza, ME Sena, BG Soares, J. Appl. Polymer Sci. 93 (2004) 1631.

98. C Su, GC Wang, F Huang, Journal of Macromolecular Science B 47 (2008) 65.

99. DM DeLongchamp, PT Hammond, Chemistry of Materials 15 (2003) 1165.

100. MF Durstock, MF Rubner, Langmuir 17 (2001) 7865.

101. JL Lutkenhaus, K McEnnis, PT Hammond, Macromolecules 40 (2007) 8367.

102. AA Antipov, GB Sukhorukov, E Donath, H Möhwald, J Phys. Chem. B 105 (2001) 2281.

103. H Ai, SA Jones, MM de Villiers, YM Lvov, Journal of Controlled Release 86 (2003) 59.

104. MP Cramer, SR Saks, Pharmacoeconomics 5 (1994) 482.

105. RD Gordon, TA Peterson, Drug Deliv. Rev. 56 (2004) 581.

106.    MC Audet, M Moreau, WD Koltun, AS Walbaum, G Shangold, AC Fisher, GE Creasy, JAMA 285 (2001) 2347.

107.    S Mitragotri, Adv. Drug. Deliv. Rev. 56 (2004) 555.

108.    KC Wood, JQ Boedicker, DM Lynn, PT Hammond, Langmuir 21 (2005) 1603.

109.    BC Ku, D Froio, D Steeves, DW Kim, H Ahn, JA Ratto, A Blumstein, J Kumar, LA Samuelson, Journal of Macromolecular Science A 41 (2004) 1401.

110.    W Jang, I Rawson, JC Grunlan, Thin Solid Films 516 (2008) 4819.

111.    CH Klute, J. Appl. Polym. Sci. 1 (1959) 340.

112.    AS Michaels, RB Parker Jr., J. Polym. Sci. 41 (1959) 53.

113.    AS Michaels, HJ Bixler, J. Polym. Sci. 50 (1961) 413.

114.    RM Barrer, JA Barrie, NK Raman, Polymer 3 (1962) 605.

115.    RM Barrer, JA Barrie, MG Rogers J. Polym. Sci. A1 (1963) 2565.

116.    JC Maxwell, Treatise on Electricity and Magnetism, Vol. I, Claredon Press, London, 1881.

117.    L Raleigh, Philos. Mag. 34 (1892) 481.

118.    EL Cussler, SE Hughes, WJ Ward, R Aris, Journal of Membrane Science 38 (1988) 161.

119.    D Perry, WJ Ward, EL Cussler, Journal of Membrane Science 44 (1989) 305.

120.    DM Eitzman, RR Melkote, EL Cussler, AIChE J. 421 (1995) 2.

121.    WR Falla, M Mulski, EL Cussler, Journal of Membrane Science 119 (1996) 129.

122.    C Yang, WH Smyrl, EL Cussler, Journal of Membrane Science 231 (2004) 1.

123.    NK Lape, EE Nuxoll, EL Cussler, Journal of Membrane Science 236 (2004) 29.

124.   PH Messersmith, EP Giannelis, Journal of Polymer Science Part A-Polymer Chemistry 33 (1995) 1047.

125.   EP Giannelis, Advanced Materials 8 (1996) 29.

126.   EP Giannelis, Applied Organometallic Chemistry 12 (1998) 675.

127.   MA Osman, JEP Rupp, UW Suter, J. Mater. Chem. 15 (2005) 1298.

128.   S Sanchez-Valdes, ML López-Quintanilla, E Ramírez-Vargas, FJ Medellín-Rodríguez, JM Gutierrez- Rodríguez, Macromol. Mater. Eng. 291 (2006) 128.

129.   MA Osman, V Mittal, M Morbidelli, UW Suter, Macromolecules 37 (2004) 7250.

130.   WH Koo, SM Jeong, Sh Choi, HK Baik, SM Lee, SJ Lee, Journal of Physical Chemistry B 108 (2004) 18884.

131.   A Choukourov, Y Pihosh, V Stelmashuk, H Biederman, D Slavinska, M Kormunda, L Zajickova, Surface & Coatings Technology 151 (2002) 214.

132.   D Li, ST Hwang, J. Membr. Sci. 66 (1992) 119.

133.   A Usuki, M Kawasumi, A Okada, Y Kojima, A Okada, T Kurauchi, O Kamigaito, J. Mater. Res. 8 (1994) 1174.

134.   Y Kojima, A Usuki, M Kawasumi, A Okada, T Kurauchi, O Kamigaito, J. Polym. Sci. Part A: Polym. Chem. 31 (1993) 983.

135.   K Yano, A Usuki, A Okada, T Karauchi, O Kamigaito, J. Polym. Sci. Part A: Polym. Chem. 31 (1993) 2493.

136.   RA Vaia, H Ishii, EP Giannelis, Chem Mater. 5 (1993) 1694.

137.   P Lebaron, Z Wang, TJ Pinnavaia, Appl. Clay Sci. 15 (1999) 12.

138.   R Krishnamoorti, EP Giannelis, Macromolecules 30 (1997) 4097.

139.   MA Osman, JEP Rupp, UW Suter, J. Mater. Chem. 15 (2005) 1298.

140. MA Osman, V Mittal, M Morbidelli, UW Suter, Macromolecules 37 (2004) 7250.

141. RA Vaia, H Ishii, EP Giannelis, Chem. Mater. 5 (1993) 1694.

142. S Nazarenko, P Meneghetti, P Julmon, BG Olson, S Qutubuddin, Journal of Polymer Science B 45 (2007) 1733.

143. A Bieder, A Gruniger, PR von Rohr, Surf. Coat. Technol. 200 (2005) 928.

144. JS Lewis, MS Weaver, IEEE J. Select. Topics Quant. Electr. 10 (2004) 45.

145. G Czeremuszkin, M Latrèche, MR Wertheimer, AS da Silva Sobrinho, Plasma Polym. 6 (2001) 107.

146. ES Lopata, Polymer Preprints 38 (1997) 1047.

147. H Chatham, Surface & Coatings Technology 78 (1996) 1.

148. M Izu, B Dotter, SR Ovshinsky, Soc. Vac. Coat. Proc. Ann. Tech. Conf. 36 (1993) 333.

149. JE Klemberg-Sapiepha, L Martinu, OM Küttel, M Wertheimer, Soc. Vac. Coat. Proc. Ann. Tech. Conf. 36 (1993) 445.

150. Y Leterrier, Prog. Mater. Sci. 48 (2003) 1.

151. AW Ott, RPH Chang, Mater. Chem. Phys. 58 (1999) 132.

152. JD Affinito, ME Gross, CA Coronado, GL Graff, IN Greenwell, PM Martin, Thin Solid Films 290-291 (1996 ) 63.

153. GL Graff, PE Burrows, RE Williford, RF Praino, Flexible Flat Panel Display Chapter 4, John Wiley & Sons, New York, 2005.

154. JD Affinito, P Martin, M Gross, C Coronado, E Greenwell, Thin Solid Films 270 (1995) 43.

155. A Yializis, DG Shaw, IEEE Trans. Comp. Hybrids Manufact. Technol. 13 (1990) 66.

156. AP Roberts, BM Henry, AP Sutton, CRM Grovenor, GAD Briggs, T Miyamoto, M Kano, Y Tsukahara, M Yanaka, J. Membrane Sci. 208 (2002) 75.

157. S Hamzehlou, AA KKatbab, Journal of Applied Polymer Science 106 (2007) 1375.

158. GM Lowman, H Tokuhisa, JL Lutkenhaus, PT Hammond, Langmuir 20 (2004) 9791.

159. AJ Nolte, MF Rubner, RE Cohen, Langmuir 20 (2004) 3304.

160. JA He, R Mosurkal, LA Samuelson, L Li, and J Kumar, Langmuir 19 (2003) 2169.

161. W Jin, A Toutianoush, B Tieke, Langmuir 19 (2003) 2550.

162. PY Vuillaume, K Glinel, AM Jonas, A Laschewsky, Chem. Mater. 15 (2003) 3625.

163. HH Rmaile, JB Schlenoff, J. Am. Chem. Soc. 125 (2003) 6602.

164. Y Maehara, S Takenaka, K Shimizu, M Yoshikowa, S Shiratori, Thin Solid Films 65 (2003) 438.

165. W Jang, JC Grunlan, Review of Scientific Instrument 76 (2005) 103904.

166. HJ Ploehn, C Liu, Ind. Eng. Chem. Res. 45 (2006) 7025.

167. DC Montgomery, GC Runger, Applied Statistics and Probability for Engineers, John Wiley & Son, New York, 1999.

168. SP Rwei, FH Ku, and KC Cheng, Colloid Polym. Sci 280 (2002) 1110.

169. K Arshak, E Moore, L Cavanagh, J Harris, B McConigly, C Cunniffe, G Lyons, S. Clifford, Compos. A: Appl Sci Manufact. 36 (2005) 487.

170. F Lux, J. Mater. Sci. 28 (1993) 285.

171. ML Clingerman, EH Weber, JA King, KH Schulz, J. Appl. Polym. Sci. 88 (2003) 2280.

172. G Yu, MQ Zhang, HM Zeng, J. Appl. Polym. Sci. 70 (1998) 559.

173. H Horibe, T Kamimura, K Yoshida, Japanese J. Appl. Phys. 44 (2005) 2025.

174. K Glinel, A Laschewsky, AM Jonas, Macromolecules 34 (2001) 5267.

175. CA Koch, JR Alchave, RK Bharadwaj, U.S. Patent No. 20040053037 A1, 18 Mar. 2004.

176. JL Lutkenhaus, EA Olivetti, EA Verploegen, BM Cord, DR Sadoway, PT Hammond, Langmuir 23 (2007) 8515.

177. K Glinel, A Laschewsky, AM Jonas, J. Phys. Chem. B 106 (2002) 11246.

178. A Ranade, NA D'Souza, B Gnade, A Dharia, J. Plast. Film Sheet. 19 (2003) 27.

179. Z Zhang, IJ Britt, MA Tung, J Appl Polym Sci. 82 (2001) 1866.

180. W Kollen, DJ Gray, J Plast Film Sheet 7 (1991) 103.

181. JC Grunlan, A Grigorian, CB Hamilton, AR Mehrabi, J Appl Polym Sci. 93 (2004) 1102.

182. JC Grunlan, A Grigorian, CB Hamilton, AR Mehrabi, J. Appl. Polym. Sci. 93 (2004) 1102.

183. JE Wong, F Rehfeldt, P Hanni, M Tanaka, RV Klitzing, Macromolecules 37 (2004) 7285.

184. J Suh, HJ Paik, BK Hwang, Bioorganic Chemistry 22 (1994) 318.

185. GM Pharr, WC Oliver, J Mater Res 7 (1992) 613.

186. MMJ Treacy, TW Ebbesen, JM Gibson, Nature 381 (1996) 678.

187. O Breuer, U Sundararaj, Polym. Compos. 25 (2004) 630.

188. TN Blanton, D Majumdar, SM Melpolder, Mater. Res. Soc. Symp. Proc. 628 (2000) CC11.14.

189. H Vali, R Hesse, H Kodama, Clays and Clay Minerals 40 (1992) 240.

190. JQ Wang, WK Chow, J. Appl. Polym. Sci. 97 (2005) 366.

191. G Guo, CB Park, YH Lee, YS Kim, M Sain, Polym. Eng. Sci. 47 (2007) 330.

192. JW Gilman, RH Harris, JR Shields, T Kashiwagi, AB Morgan, Polym. Adv. Technol. 17 (2006) 263.

193. M Si, M Goldman, G Rudomen, MY Gelfer, JC Sokolov, MH Rafailovich, Macromol. Mater. Eng. 291 (2006) 602.

194. L Song, Y Hu, Y Tang, R Zhang, Z Chen, W Fan, Polym. Degrad. Stab. 87 (2005) 111.

195. M Bartholmai, B Schartel, Polym. Adv. Technol. 15 (2004) 355.

196. J Zhu, P Start, KA Mauritz, CA Wilkie, Polym. Degrad. Stab. 77 (2002) 253.

197. JM Brown, D Curliss, RA Vaia, Chem. Mater. 12 (2000) 3376.

198. S Peeterbroeck, F Laoutid, B Swoboda, JM Lopez-Cuesta, N Moreau, JB Nagy, M Alexandre, P Dubois, Macromol. Rapid Commun. 28 (2007) 260.

199. B Schartel, P Potschke, U Knoll, M Abdel-Goad, Eur. Polym. J. 41 (2005) 1061.

200. T Kashiwagi, E Grulke, J Hilding, R Harris, W Awad, J Douglas, Macromol. Rapid Commun. 23 (2002) 761.

201. T Kashiwagi, F Du, JF Douglas, KI Winey, RH Harris, JR Shields, Nature Mater. 4 (2005) 928.

202. YS Song, JR Youn, Carbon 43 (2005) 1378.

203. JD Jacobs, H Koerner, H Heinz, BL Farmer, P Mirau, PH Garrett, RA Vaia, Journal of Physical Chemistry B 110 (2006) 20143.

204. P Wang, CY Tan, YG Ma, WN Cheng, CK Ong, Microwave and Optical Technology Letters 50 (2008) 566.

**APPENDIX A**

**ANALYSIS OF VARIANCE [200]**


**A.1 Thickness Comparison of Hand Dipping and Robot Dipping**

A widely used statistical method called analysis of variance (ANOVA) is used to prove the significance of regression.

$$\sum_{i=1}^{n}(y_i - \bar{y})^2 = \sum_{i=1}^{n}(\hat{y}_i - \bar{y})^2 + \sum_{i=1}^{n}(y_i - \hat{y}_i)^2 \qquad \text{A-1}$$

The first term of the right side of equation A-1 is the regression sum of squares ($SS_R$) and the second term is the error sum of squares ($SS_E$). The left side of equation A-1 is the total corrected sum of squares ($SS_T$).

There are several kinds of ANOVA, for example, one-way ANOVA, two-way ANOVA, MANOVA, ANCOVA, etc. Two-way ANOVA was conducted for the thickness and sheet resistance comparison between hand dipping and robot dipping. There are two independent variables, number of bilayers and dipping methods (hand dipping and robot dipping). The governing equation is:

$$Y_{ij}=\mu+\tau_i+\beta_j+(\tau\beta)_{ij} \quad i=1, 2, 3, 4, 5, 6 \ \ j=1, 2 \qquad \text{A-2}$$

where $\tau_i$ is the effect of the number of bilayers, $\beta_j$ is the effect of dipping methods, and $(\tau\beta)_{ij}$ is the effect of interaction. If the effect of interaction is non-zero, the actual effect, $Y_{ij}$, cannot be the superposition of the effects of the number of bilayers and dipping methods.

There are two hypotheses, class B and class D. The class B (number of bilayers effect) hypothesis is

$H_0: \tau_1 = \tau_2 = \tau_3 = \tau_4 = \tau_5 = \tau_6$

$H_a$: Not $H_0$

The class D (dipping methods effect) is

$I_0: \beta_1 = \beta_2$

$I_a: \beta_1 \neq \beta_2$

**Table A-1** The properties of classes B and D.

| Class | Levels | Values |
|-------|--------|--------|
| B | 6 | 5, 10, 15, 20, 25, 30 |
| D | 2 | 1, 2 |

Analyzed results are described in Table A-2. The B*D value is smaller than the critical value, (0.0001), suggesting that $(\tau\beta)_{ij}$ is indeed non-zero. The hypothesis $H_0$ should be rejected. We do not need to analyze the main effects B and D.

**Table A-2** Results of the class B and D hypotheses.

| Source | DF | Type III SS | Mean Square | F Value | Pr > F |
|--------|----|-------------|-------------|---------|--------|
| B | 5 | 1828184.763 | 365636.953 | 17211.4 | < 0.0001 |
| D | 1 | 192.257 | 192.257 | 9.05 | 0.0048 |
| B*D | 5 | 947.633 | 189.527 | 8.92 | < 0.0001 |
| Error | 36 | 764.779 | 21.244 | | |

Table A-3 is the results of analyzed interaction effects. The results indicate that hand dipping and robot dipping have no difference, except for the 30th bilayer, where the least square means for the effect of B*D is smaller than the critical value.

**Table A-3** Least Square Means for effect B*D, Pr > |t| for H0: LSMean (i) = LSMean (j).

| i/j | 1 | 2 | 3 | 4 | 5 | 6 | 7 | 8 | 9 | 10 | 11 | 12 |
|---|---|---|---|---|---|---|---|---|---|---|---|---|
| 1 | | 1 | <0.0001 | <0.0001 | <0.0001 | <0.0001 | <0.0001 | <0.0001 | <0.0001 | <0.0001 | <0.0001 | <0.0001 |
| 2 | 1 | | <0.0001 | <0.0001 | <0.0001 | <0.0001 | <0.0001 | <0.0001 | <0.0001 | <0.0001 | <0.0001 | <0.0001 |
| 3 | <0.0001 | <0.0001 | | 0.9979 | <0.0001 | <0.0001 | <0.0001 | <0.0001 | <0.0001 | <0.0001 | <0.0001 | <0.0001 |
| 4 | <0.0001 | <0.0001 | 0.9979 | | <0.0001 | <0.0001 | <0.0001 | <0.0001 | <0.0001 | <0.0001 | <0.0001 | <0.0001 |
| 5 | <0.0001 | <0.0001 | <0.0001 | <0.0001 | | 0.8336 | <0.0001 | <0.0001 | <0.0001 | <0.0001 | <0.0001 | <0.0001 |
| 6 | <0.0001 | <0.0001 | <0.0001 | <0.0001 | 0.8336 | | <0.0001 | <0.0001 | <0.0001 | <0.0001 | <0.0001 | <0.0001 |
| 7 | <0.0001 | <0.0001 | <0.0001 | <0.0001 | <0.0001 | <0.0001 | | 0.9556 | <0.0001 | <0.0001 | <0.0001 | <0.0001 |
| 8 | <0.0001 | <0.0001 | <0.0001 | <0.0001 | <0.0001 | <0.0001 | 0.9556 | | <0.0001 | <0.0001 | <0.0001 | <0.0001 |
| 9 | <0.0001 | <0.0001 | <0.0001 | <0.0001 | <0.0001 | <0.0001 | <0.0001 | <0.0001 | | 0.9965 | <0.0001 | <0.0001 |
| 10 | <0.0001 | <0.0001 | <0.0001 | <0.0001 | <0.0001 | <0.0001 | <0.0001 | <0.0001 | 0.9965 | | <0.0001 | <0.0001 |
| 11 | <0.0001 | <0.0001 | <0.0001 | <0.0001 | <0.0001 | <0.0001 | <0.0001 | <0.0001 | <0.0001 | <0.0001 | | <0.0001 |
| 12 | <0.0001 | <0.0001 | <0.0001 | <0.0001 | <0.0001 | <0.0001 | <0.0001 | <0.0001 | <0.0001 | <0.0001 | <0.0001 | |

## A.2 Sheet Resistance Comparison of Hand Dipping and Robot Dipping

Two-way ANOVA was also used to analyze the sheet resistance comparison in Chapter III. $\tau_i$ is the effect of the number of bilayers, $\beta_j$ is the effect of dipping methods, hand dipping and robot dipping, and $(\tau\beta)_{ij}$ is the effect of interaction. There are two hypotheses, class B and class D. The class B (number of bilayers effect) hypothesis is:

$H_0$: $\tau_6=\tau_8=\tau_{10}$

$H_a$: Not $H_0$

The class D (dipping methods effect) is:

$I_0$: $\beta_1=\beta_2$

$I_a$: $\beta_1\neq\beta_2$

**Table A-4** The properties of classes B and D.

| Class | Levels | Values |
|---|---|---|
| B | 3 | 6, 8, 10 |
| D | 2 | 1, 2 |

Analyzed results are described in Table A-5. The B*D value is greater than the critical value, suggesting there is no effect of interaction. The hypothesis $H_0$ should be

accepted. We do not need to analyze the main effects B*D. The effect of the number of

bilayers is the only factor to change the thickness of the film.

**Table A-5** Results of the class B and D hypotheses.

| Source | DF | Type III SS | Mean Square | F Value | Pr > F |
|--------|-----|-------------|-------------|---------|----------|
| B | 2 | 1494821750 | 745910875 | 242.98 | < 0.0001 |
| D | 1 | 2130495 | 2130495 | 0.69 | 0.4157 |
| B*D | 2 | 799302 | 399651 | 0.13 | 0.8787 |
| Error | 18 | 55256271 | 3069793 | | |

# APPENDIX B

## ONE SAMPLE t-TEST [200]

### B.1 Mechanical Properties of PEI/MMT Assemblies.

A sample mean of the measured modulus in Chapter V was examined. The hypothetical mean value is 2 MPa, which is the modulus of the normal polymer. A one sample t-test was used to prove the improvement of modulus. The hypothesis is:

$H_0$: $\mu = \mu_0$

$H_a$: $\mu > \mu_0$, $\mu < \mu_0$, $\mu \neq \mu_0$

The governing equation of the t value is

$$t = (\mu_0 - \mu)/S_{\mu 0} \qquad\qquad B\text{-}1$$

where $\mu_0$ is the hypothetic mean (2 MPa) and $\mu$ is the mean value of samples. $S_{\mu 0}$ is the standard error of the mean.

**Table B-1.** The modulus of pH 8 and pH 9 systems.

|  | Modulus (GPa) | |
|---|---|---|
|  | pH 8 | pH 9 |
| AVG. | 18.35 | 11.40 |
| STDEV | 9.76 | 3.21 |
| t Value | 6.04 | 9.69 |

Table B-2 summarizes the test results. The significance levels of pH 8 and 9 are smaller than 0.0001. Therefore, the modulus of pH 8 and pH 9 systems is improved from the neat polymer.

**Table B-2.** Results of the t-test.

|       | t        | DF | Significant Level | Mean Difference |
|-------|----------|----|-------------------|-----------------|
| pH 8  | 6.040228 | 12 | < 0.001           | 16.3484         |
| pH 9  | 9.69467  | 10 | < 0.001           | 9.39586         |

**VITA**

Name:                    Woo-Sik Jang

Address:              680 Mix Ave. #5F Hamden, TX. 06515

Email Address:    jangw428@gmail.com

Education:         B.S., Mechanical Engineering, Korea University, 2000.

M.S., Mechanical Engineering, Univeristy of Colorado at Boulder 2003

Career:               H.V.A.C. Design Engineer, Hyundai Engineering and Construction Company 2001

Publication:       T. Dawidczyk, M. D. Walton, W. S. Jang, J. C. Grunlan, "Layer-by-Layer Assembly of UV-Resistant Poly(3, 4 Ethylenedioxythiophene) Thin Film," Langmuir 24 (2008) 8314.

W. S. Jang, I. M. Rawson, J. C. Grunlan, "Layer-by-Layer Assembly of Thin Film Oxygen Barrier," Thin Solid Films 516 (2008) 4819.

W. S. Jang, J. C. Grunlan, "Robotic Dipping System for Layer-by-Layer Assembly of Multifunctional Thin Films," Rev. Sci. Instr. 76 (2005), 103904.